Publications of the Astronomical Society of Australia (2026), **43**, e121, 20 pages
doi:10.1017/pasa.2026.10248

CAMBRIDGE UNIVERSITY PRESS

Research Article

The Hα specific angular momentum of dwarf galaxies

Simon Richard Deeley[1], Sarah Sweet[1,2], Dilyar Barat[3], Matthew Colless[2,3], Luca Cortese[2,4] and Francesco D'Eugenio[5,6]

[1]School of Mathematics and Physics, The University of Queensland, Australia, [2]ARC Centre of Excellence for All Sky Astrophysics in 3 Dimensions (ASTRO 3D), Canberra, Australia, [3]Research School of Astronomy & Astrophysics, Australian National University, Australia, [4]International Centre for Radio Astronomy Research (ICRAR), University of Western Australia, Crawley, WA, Australia, [5]Kavli Institute for Cosmology, University of Cambridge, UK and [6] Cavendish Laboratory - Astrophysics Group, University of Cambridge, Cambridge, UK

Abstract

The relationship between a galaxy's specific angular momentum j and its mass M, parameterised by $j \propto M^{\alpha}$ and known as the Fall relation, has emerged as a fundamental scaling relation reflecting key physical and morphological properties of galaxies. This relation has been well studied for galaxies with masses above 10^9 $M_{\odot}$. However, whether or not it holds for the low-mass dwarf galaxies, especially given their varied morphologies, remains uncertain. Here we use Hα observations of 49 star-forming dwarf galaxies from the SHαDE survey, as well as 20 high-mass 'control' galaxies, to investigate the stellar j_*–M_* relation down to masses below 10^6 $M_{\odot}$. We find that the star-forming dwarf galaxies follow the same j_*–M_* relation as high-mass disc-like galaxies, with $\alpha = 0.53 \pm 0.4$, demonstrating that the relation holds across 5 orders of magnitude in mass. We then select a matching sample from the IllustrisTNG cosmological simulation and create mock observations resembling the SHαDE survey. We find that the simulated dwarf galaxy population follows the extrapolated j_*–M_* relation with a flattening and significant scatter towards lower j_* values. Following the evolution of these galaxies, we find that dwarf galaxies experience a gradual loss in j_* with time, while high-mass galaxies experience a sudden jump in j_* before settling into a stable state. This dynamical evolution leads to a redshift dependence in α, with $\alpha = 0.45$ at $z = 2$ and 0.55 at $z = 0$. Despite the apparent simplicity in the present-day j_*–M_* relation over a wide mass range, the evolution of j leading to this relation is complex and dynamic.

Keywords: Galaxies: dwarf; galaxies: evolution; galaxies: kinematics and dynamics; galaxies: structure

(Received 28 November 2025 UTC; revised 7 July 2026 UTC; accepted 28 July 2026 UTC)

1. Introduction

One of the most important aspects in our understanding of galaxy evolution is how galaxies initially acquired their angular momentum and how this angular momentum evolved over time, leading to the diversity of galaxy structures we observe today. By our current understanding, in the early Universe gravitational forces from neighbouring over-densities created a tidal torque on each halo, acting to gradually increase their angular momentum as they continued to grow in mass through accretion and in size with the expanding Universe (Hoyle 1949). This continued until the inward gravitational force out-competed the rate of expansion and the halos began to collapse, at which point the strength of the tidal forces greatly reduced, effectively freezing in the halo's angular momentum (J) at that time. The time at which this 'turnaround' occurred, and hence the angular momentum gained, was dependent on the halo's mass, leading to an expected relation between the halo's mass and its specific angular momentum $j \propto M^{\alpha}$, where $j = J/M$ and M is the halo mass. Peebles (1969) analytically derived a value of 2/3 for the parameter α, and additional analytical approaches were carried out by Doroshkevich (1970) and White (1984). This was tested in numerical simulations by Efstathiou & Jones (1979) and found to be in agreement with the expected relation.

As the gas within the halo collapses further into the centre and forms the central galaxy, the forming galaxy and its stars should then (at least in an idealised closed-box scenario where the halo angular momentum is conserved) have the same angular momentum as the host halo. The mass-angular momentum of the dark matter halo would therefore be reflected in a mass-angular momentum relation of the central galaxies, which we are able to observe and measure. The first observational test of this relation was made by Fall (1983), who found that galaxies do indeed follow a j_*–M_* relation with $\alpha = 0.55$, where j_* and M_* refer to the stellar component of j and the stellar mass, respectively. This relation is now commonly referred to as the Fall relation. As detailed below, a growing number of studies have since confirmed this relationship and explored how it varies with morphology and bulge/disc components.

Studies have revealed a fundamental connection between the j–M relation and the morphology of galaxies. While the value of α remains largely independent of galaxy morphologies, the normalisation of this relation is found to be morphology-dependent. Spiral galaxies have the highest j_* for a given mass, while elliptical galaxies have j_* values a factor of 5 times lower (Romanowsky & Fall 2012). More generally, there is a clear trend of decreasing j_* from late-type disc galaxies through lenticular galaxies to early-type elliptical galaxies (Cortese et al. 2016). There is also

Corresponding author: Simon Richard Deeley; Email: s.deeley@uq.edu.au

Cite this article: Deeley SR, Sweet S, Barat D, Colless M, Cortese L and D'Eugenio F. (2026) The Hα specific angular momentum of dwarf galaxies. *Publications of the Astronomical Society of Australia* **43**, e121, 1–20. https://doi.org/10.1017/pasa.2026.10248

© The Author(s), 2026. Published by Cambridge University Press on behalf of Astronomical Society of Australia. This is an Open Access article, distributed under the terms of the Creative Commons Attribution licence (https://creativecommons.org/licenses/by/4.0/), which permits unrestricted re-use, distribution and reproduction, provided the original article is properly cited.

a strong related connection between j_* and the bulge mass fraction; galaxies with a large bulge have lower j_* values relative to those with smaller bulges (Obreschkow & Glazebrook 2014). In fact, bulges and discs, when separated from each other, are each found to independently follow parallel j_*–M_* relationships, with the bulges having lower j_* relative to the discs (being closer in line with elliptical galaxies) (Fall & Romanowsky 2018). The bulge type is also important, with galaxies that host rotating pseudobulges tending to have lower bulge fraction for a given j_*/M_* than galaxies that host classical bulges (Sweet et al. 2018). The fundamental relationship between a galaxy's angular momentum and its morphology has been proposed as an alternative, physically motivated way to classify galaxies in place of the visual component-based system widely used today (Sweet et al. 2020).

An additional physical property that has been found to be reflected in the j–M relation is the galaxy's gas mass fraction. Mancera Piña et al. (2021*a*) studied an amalgamated sample of 157 galaxies with neutral HI gas rotation curves and found $\alpha = 0.54$, 1.02, and 0.6 for the stellar, gas, and baryonic (star + gas) components respectively, finding that the stellar and baryonic j is higher for galaxies with higher gas mass fractions. Mancera Piña et al. (2021*b*) found that by incorporating the gas mass fraction, they were able to produce a tight 3D relationship between galaxy mass, gas mass fraction and specific angular momentum, with galaxies containing higher gas mass fractions featuring higher angular momenta. Using a sample of 559 galaxies observed through their HI emission, Hardwick et al. (2022) also found that the scatter in the j_*–M_* relation is largely explained by the fraction of neutral gas in the galaxies, with galaxies containing a higher fraction of HI gas again having higher values of j_*. This observed gas-fraction relationship was found to be reproduced by both the EAGLE and IllustrisTNG simulations, with the two simulations being in close agreement with each other (Hardwick et al. 2023).

The j_*–M_* relation obtained from observed galaxies has been successfully reproduced within various cosmological simulations. Using the Illustris TNG100 simulation, Rodriguez-Gomez et al. (2022) found a j_*–M_* relation that agrees with observations down to masses of 10^9 $M_*(\mathrm{M}_\odot)$, including the observed lower j_* for ellipticals relative to spirals, and further concluded that the baryonic component retains 50–60% of their host halo's angular momentum in spiral galaxies and 10–20% in elliptical galaxies. Elson et al. (2023), using the SIMBA cosmological simulation, also found a j_*–M_* relation consistent with a single power law down to galaxy masses of 10^8 $M_*(\mathrm{M}_\odot)$, finding that galaxies with a higher mass of HI gas have higher angular momentum, in agreement with the observations detailed above. Lagos et al. (2017) showed that the j_*–M_* relation is reproduced within the EAGLE cosmological simulation. These simulations can therefore be used to investigate how the evolutionary history of galaxies impacts their final j_* values.

The final angular momentum of a galaxy may be significantly influenced by the timing of the initial build-up of its mass and stars. Using EAGLE, Zavala et al. (2016) showed that for galaxies that formed all their stars before the point at which the host halo begins to contract in size (the turnaround point), the stars subsequently lose their angular momentum due to merger activity during the continued build-up of the inner halo. Stars that form after this turnaround point do so from high-angular-momentum gas falling in from the halo's outskirts, resulting in a stellar disc with high angular momentum.

It has been seen that subsequent galaxy evolution may further alter the amount of angular momentum measured in galaxies today. As already mentioned, elliptical galaxies have lower j_* values and are believed to have formed through highly disruptive merger events. Lagos et al. (2018) used the EAGLE simulation to investigate the impact of mergers on j_*, finding that both major and minor mergers can significantly alter a galaxy's angular momentum. Mergers with galaxies containing little gas ('dry mergers') caused a greater loss of j_*, while prograde gas-rich mergers were able to spin up the galaxy. In addition, they found that early quenching of star formation also results in a galaxy with lower j_* and an elliptical morphology. Using the Illustris simulation, Genel et al. (2015) also found major mergers to reduce a galaxy's angular momentum and additionally found j_* to be influenced by gas flows. Galactic outflows of gas, driven by outward pressure from star-forming regions, preferentially removes gas with lower angular momentum. This gas flows out into the outer halo where it can regain angular momentum from the halo's outskirts, before cooling and falling back in towards the galaxy. Meanwhile, an alternative pathway for galaxy quenching, namely the infall of galaxies into dense cluster environments, may leave the j_*–M_* relation largely unaffected (Mostoghiu et al. 2021). Given the wide range of complex histories and environments experienced by each individual galaxy, it is still not well understood why they fall onto a tight relation between their mass and angular momentum, and why the slope of this relation is retained despite large changes in j after dramatic morphological transformations.

Whether or not the j_*–M_* relation extends down to the dwarf galaxies has not yet been fully resolved. One of the most comprehensive observational studies into the Fall relation was carried out by Posti et al. (2018), who looked at the stellar kinematics of 92 disc galaxies with masses between 10^7 and 10^{11} $M_*(\mathrm{M}_\odot)$ and found a tight j_*–M_* relation with $\alpha = 0.66$. However, their sample included only six galaxies below 10^8 $M_*(\mathrm{M}_\odot)$. Most studies of dwarf galaxies to date have focused on their HI components, due to the gas-rich nature of these systems and the extension of HI observations to larger radii. Butler et al. (2017) measured the angular momentum of dwarf galaxies between 10^6 and 10^9 $M_*(\mathrm{M}_\odot)$, finding that they had higher angular momentum than expected from an extrapolation of the relation found for larger spirals. They argued that this may be due to the higher mass-to-light ratio of dwarf galaxies. Kurapati et al. (2018) extended this to isolated dwarf galaxies located in voids and again found a higher degree of angular momentum for these galaxies. When combining with high-mass galaxies in previous work, they saw evidence for a transition in momentum at a mass of $10^{9.1}$ $M_*(\mathrm{M}_\odot)$, with galaxies below this threshold mass exhibiting higher angular momentum. Chowdhury & Chengalur (2017) measured j for 5 dwarf galaxies between $10^{7.5}$ and 10^9 $M_*(\mathrm{M}_\odot)$ and again found a higher j then predicted from the extrapolation. Both Elson (2017) and Mancera Piña et al. (2021*a*) meanwhile found no divergence from the relation for galaxies between 10^7 and 10^{11} $M_*(\mathrm{M}_\odot)$. Specifically, Mancera Piña et al. (2021*a*) tested for a broken power law in the relation and found that the sample was better explained using a single power law. Alternatively, any change in the j_*–M_* relation among dwarf galaxies may arise from an offset in the absolute values rather than a change in slope, as is the case for the spiral and elliptical galaxies. A larger sample of dwarfs over a wide mass range would be needed to reveal such an offset.

Most of these studies assume that dwarf galaxies are pure rotating discs, and while hydrogen traces well the smooth disc out to large radii, it is not sensitive to small-scale kinematic features within the star-forming optical extent. Here we use an alternative tracer of specific angular momentum in dwarf galaxies. With many

https://doi.org/10.1017/pasa.2026.10248 Published online by Cambridge University Press

dwarf galaxies being gas-rich star-forming systems, the bright Hα emission line offers an ideal alternative to accurately trace their specific angular momenta in these otherwise faint galaxies. Hα emission has been used previously to study the j_*–M_* relation of higher-mass galaxies; for example, Cortese et al. (2016) used the SAMI Galaxy Survey to derive the j–M relation for both the stellar and Hα component. However, even the relatively high spectral resolution of the SAMI spectroscopy ($R = 4\,263$ at $H\alpha$, corresponding to a velocity resolution of 30 km s^{-1}) is insufficient to accurately measure the velocity dispersion in low-mass dwarf galaxies (Barat et al. 2020), except for the few, highest-quality observations (Zhou et al. 2017). To address this limitation, here we use spatially-resolved spectroscopy targeting warm ionised gas emission with high spectral resolution to measure j_* in a sample of low-mass galaxies, testing the extension of the j_*–M_* relation into the dwarf galaxy regime. Throughout this paper we assume a cosmological constant plus cold dark matter cosmology (ΛCDM) with $\Omega_M = 0.3$, $\Omega_\Lambda = 0.7$, and $H_0 = 70$ km s^{-1}, and a Chabrier initial mass function (Chabrier 2003).

2. Data

In this work we combine an observational survey of star-forming dwarf galaxies with a sample taken from the IllustrisTNG-50 cosmological simulation in order to further explore the extension of the Fall relation to low-mass galaxies. Below we outline the galaxy samples used for each of these two components.

2.1. Observational sample

To investigate the angular momentum of dwarf galaxies in the local Universe we use data from the Study of Hα from Dwarf Emissions (SHαDE) survey (Barat et al. 2020). The SHαDE survey was designed to extend existing large integral field unit (IFU) surveys such as SAMI, which target bright high-mass galaxies, into the low-mass dwarf galaxy regime. The aims of the survey were to investigate the extension of scaling relations into the low-mass regime, the accretion of angular momentum, the asymmetry of dwarf galaxy kinematics and the dynamical impact of star formation.

The complete details of the SHαDE survey are presented in Barat et al. (2020). In summary, the SHαDE survey targeted 49 dwarf galaxies within a stellar mass range of $10^5 \leq M_*(\mathrm{M}_\odot) \leq 10^{8.5}$ and with apparent angular sizes in the range $1.2 \leq R_d(\mathrm{arcsec}) \leq 11$. To ensure their kinematics could be accurately measured through their Hα emission, their total Hα fluxes were required to be above 5×10^{-16} ergs s^{-1} cm^{-2} Å arcsec^{-2}. This requirement resulted in the sample consisting of star-forming dwarf galaxies; Figure 2 shows the location of this sample (purple points) compared to established relationships between mass and star formation rate.

As part of the SHαDE survey, a sample of 20 'control' galaxies within the stellar mass range of $10^{8.5} \leq M_*(\mathrm{M}_\odot) \leq 10^{10.5}$ (selected from the SAMI survey) were also included, allowing us to verify the consistency of our methods with previous work and to test with a consistent sample whether scaling relations found amongst the high-mass galaxies can be continuously extended down to the dwarf galaxy population. The complete observational sample is listed in Table 1.

All 69 galaxies were observed with the FLAMES/GIRAFFE IFU instrument on the Very Large Telescope using the GIRAFFE spectrograph in 'Argus' mode, a single IFU consisting of 22×14 microlenses, with each lens covering 0.52 arcsec on the sky. This results in a 11.4×7.3 arcsec^2 array of 308 spectra. From the measured spectrum within each spaxel, pPXF (Cappellari 2023) was used to measure the velocity and velocity dispersion from the Hα emission line, resulting in 2D maps of the velocity and velocity dispersion for each galaxy.

galaxies have been imaged by the Hyper-Suprime Cam Subaru Strategic Program survey (Aihara et al. 2018), allowing a detailed view of their morphology. We used the g, i, and r-band images to construct red-green-blue colour images for these galaxies, eight of which are shown in Figure 1. These examples highlight the range of morphologies in our sample, which includes very disky galaxies as well as highly irregular and clumpy galaxies. Owing to the selection of galaxies with high Hα flux, all these galaxies are blue star-forming galaxies, with many featuring prominent clumps and regions of ongoing star formation. Four of the higher-mass control galaxies are also shown in Figure 1. The full sample of galaxies has been imaged by the DESI Legacy Imaging Surveys (Dey et al. 2019), which we have used to visually classify the morphology of each galaxy as either disc-like, irregular, or compact (i.e. having either a very compact or unresolvable structure).

2.2. Simulation sample

For the simulation comparison, we used the IllustrisTNG cosmological simulation (Nelson et al. 2018, 2019b; Marinacci et al. 2018; Naiman et al. 2018; Pillepich et al. 2018; Springel et al. 2018). We specifically use the smallest-volume, highest-resolution TNG50 simulation (Nelson et al. 2019*a*,*b*; Pillepich et al. 2019) in order to allow us to more finely resolve low-mass dwarf galaxies. The simulation's volume is 51.7 Mpc^3, allowing for the study of galaxies in a wide range of environments with the largest structures being of similar size to the Virgo galaxy cluster. The simulation features particle resolutions for baryonic and dark matter particles of 8.5×10^4 M$_\odot$ and 4.5×10^5 M$_\odot$, respectively.

The crucial benefit in using TNG50 for this work is the ability to study dwarf galaxies and their acquisition of angular momentum within a broader cosmological context and to consistently compare these galaxies to high-mass disc galaxies in the same context. In particular, TNG50 offers the highest resolution currently available while maintaining such a cosmologically-relevant context. We note that we are approaching the limits of what the simulation can reliably resolve, meaning that resolution effects may have an influence on our findings. For example, potential influences on galaxy structure have been identified by Celiz et al. (2025), namely a flattening of the mass-radius relation below 10^8 M_*(M$_\odot$). However, as we will further detail below, we also note that the dynamical transitions we see within our simulation results are consistent with higher resolution zoom-in simulations (Benavides et al. 2025), and we find consistent results within the lower-resolution TNG100 simulation. While these comparisons suggest TNG50 can still produce dynamical processes for such low-mass galaxies, we stress that potential resolution effects should be kept in mind through the rest of this paper.

From this simulation we selected a sample of 512 galaxies in the stellar mass range $10^6 \leq M_*(\mathrm{M}_\odot) \leq 10^{10.5}$. Due to the increased computational time for deriving observational maps for high-mass galaxies and the focus of this work on testing the Fall relation within the dwarf galaxy regime, we have over-sampled below 10^8 M$_\odot$ relative to the higher-mass galaxies. We then applied a further selection cut based on star formation rate (SFR), reflecting the minimum Hα emission requirement of our observational sample. This minimum effectively corresponds to a lower limit in star

https://doi.org/10.1017/pasa.2026.10248 Published online by Cambridge University Press

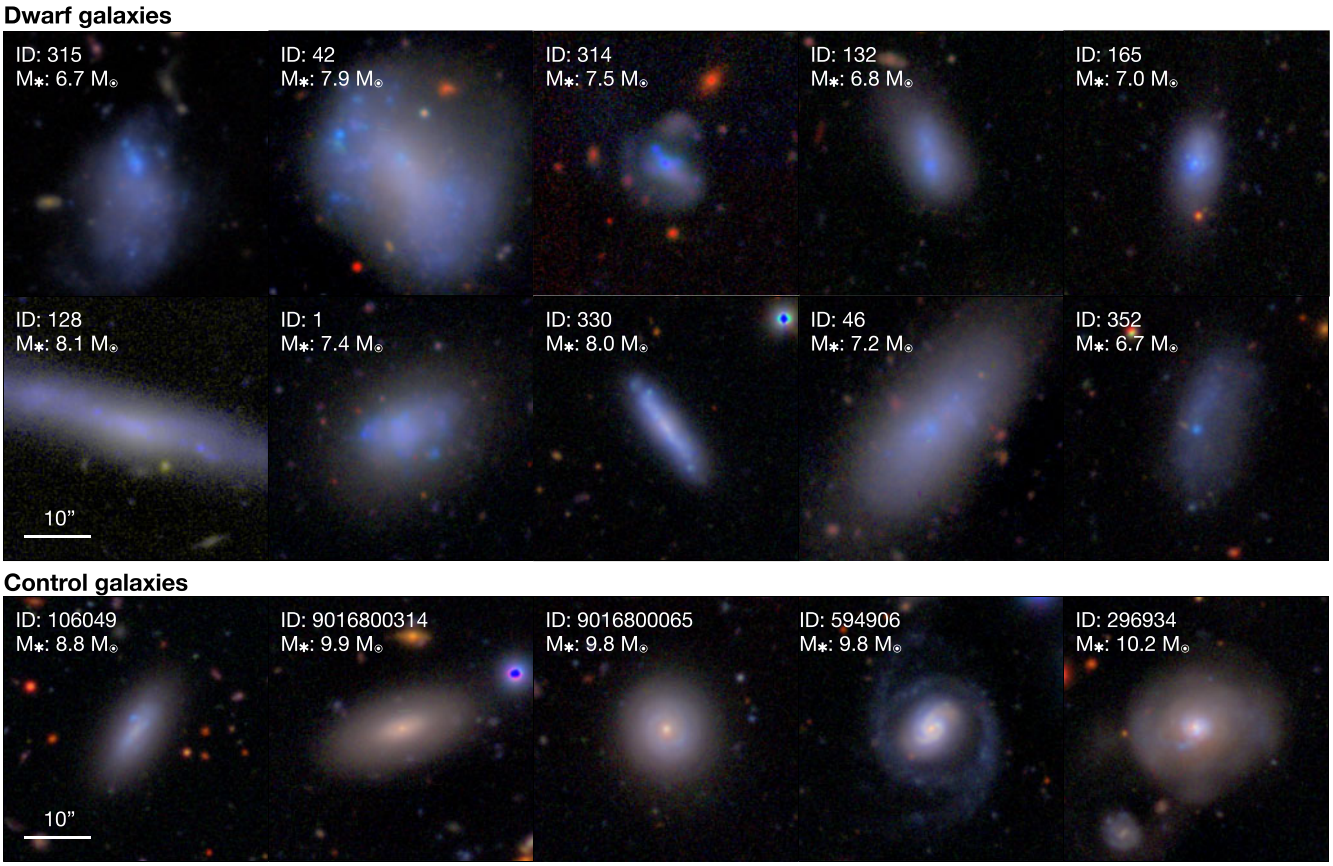


Figure 1. HSC imaging of dwarf galaxies (top two rows) and higher-mass control galaxies (bottom row). The dwarf galaxy sample includes a wide range of galaxy morphologies, from highly irregular and clumpy galaxies to thin, well-organised discs. The blue colours reflect the Hα flux selection of these galaxies, and therefore their high star formation rates. The control sample, meanwhile, consists mainly of large disc galaxies. The scale bars in the lower left of each row indicates 10 arcsec. Note that the control galaxies are located further away such that they are contained within the same instrumental field of view.

formation (Kennicutt 1998*b*), with all except four of our observed galaxies having $\log_{10}$ (SFR) > -3; we therefore use this SFR as a lower limit for our simulation sample. This fixed SFR limit results in the preferential removal of galaxies with low star formation at lower masses relative to higher masses. Investigating the mass-SFR distribution of our sample shows that this begins to bias the simulation sample below $10^7 \leq M_*(\mathrm{M}_\odot)$. The mass-SFR distribution of the simulation sample is shown in Figure 2 as the blue points.

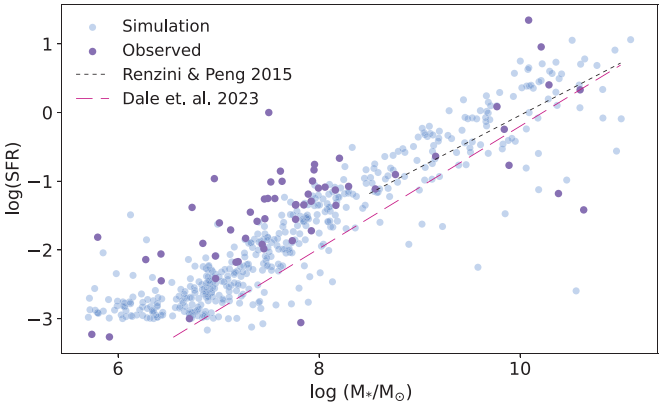


Figure 2. The star-forming sequence of our simulation sample (blue) compared to our observational sample (purple). For comparision, the star-forming main sequence found by Renzini & Peng (2015) for galaxies above $10^{8.5}$ $\mathrm{M}_\odot$ and for local-volume galaxies down to 10^6 $\mathrm{M}_\odot$ (Dale et al. 2023) is shown. Below $10^{6.5}$ $\mathrm{M}_\odot$, the sample becomes biased towards higher star formation rates due to our selection limits.

3. Methods

3.1. SHαDE

To calculate j_* we follow the methods of Sweet et al. (2020), combining robust observational kinematic and surface density maps with a model extrapolation to 3 effective radii.

3.1.1. Kinematics

Firstly, in order to correctly model the velocity field, we removed spaxels with high uncertainties or unphysical values while avoiding the removal of spaxels with valid and important information. We began by removing all spaxels with a signal-to-noise ratio $\leq$5. To remove remaining spaxels with large uncertainties without significantly reducing the number of available pixels for analysis, we also removed those with a line-of-sight velocity uncertainty greater than 30 km s^{-1}. After these initial cuts, isolated high-velocity spaxels remained in a number of kinematic maps, many of which had velocity values that deviated significantly from the rest of the map. In addition, there were a

https://doi.org/10.1017/pasa.2026.10248 Published online by Cambridge University Press

number of spaxels with velocity signs opposite to all neighbouring spaxels. We tested two methods to remove these outliers. The first method involved sigma clipping, where we removed all spaxels with velocities more than 2.5 standard deviations from the mean. While this successfully removed all isolated and contrary spaxels, it had the undesirable side-effect of removing high-velocity clumps that were clearly real features of the galaxy's velocity field. The second method involved removing all spaxels with no neighbours or with all surrounding spaxels having the opposite sign. While this left some spaxels with highly divergent velocities, it retained the important features of the velocity fields. We carried out the analysis using both methods and found that, aside from some shifts in j for individual galaxies, the overall j–M_* relations were virtually unchanged between the two approaches; for the remainder of this paper we present results using only the second method.

We then deprojected the velocity fields and created a kinematic model of each galaxy assuming a thin, axisymmetric exponential disc. We use the continuum flux map to determine the inclination and the line-of-sight velocity map to find the kinematic centre and position angle, from which we determined the deprojected radius and velocity of each spaxel. We then fitted the radial velocity profile with an exponential profile and from this created a model velocity field. We test the assumption of a thin kinematic disc and our method of deprojection in Section 4.3 by (alternatively) deprojecting the line-of-sight velocities using optically derived ellipticities and varying the assumed disc thickness (parametrised by q_0), finding that our results remain consistent when using this alternative approach.

3.1.2. Calculation of j_*

To arrive at a measure of the stellar angular momentum, which requires both a measure of the stars' motions and mass distribution, we use the kinematics derived from the Hα emission-line maps (see Barat et al. 2020 for how these maps were created) and assume that the stellar mass distribution follows the galaxy's continuum optical flux. While reflecting the dynamics of younger stellar populations, we note that, in using the kinematics of star-forming regions, this approach may result in j values that vary from the broader stellar population, particularly an older population that may have formed under different dynamical circumstances and subsequently been influenced by evolutionary processes such as mergers. This should be kept in mind when interpreting the results of this paper and in making comparisons to other work.

In modelling the continuum-derived stellar mass distribution, we assume the distribution to take the form of an exponential disc and normalise the total continuum flux by the galaxy's total mass. Using the deprojected velocities derived from the kinematic modelling above, we then go through all N spaxels and calculate the observational j_* by

$$j_* = \frac{\sum_{i=0}^{N} M_i v_i r_i}{\sum_{i=0}^{N} M_i}, \tag{1}$$

where M_i is the mass, r_i is the radius, and v_i is the deprojected line-of-sight velocity of the ith spaxel. In addition, we also calculate j_* for all galaxies using the velocity field of the best fitting disc model, restricted to within 3 effective radii (R_e); we call this $j_{*\mathrm{model}}$. Finally, we use the model velocity field to fill in missing spaxels in the observational map to create a combined model + observational velocity map and calculate a combined j value ($j_{*\mathrm{total}}$) (again out to a limit of $3R_e$ for all galaxies). While including the model mass and velocity field for galaxies that are approaching convergence systematically increases the absolute value of j_* due to the filling in of spaxels which otherwise have no observational data, we find that our main conclusions are not significantly affected by the choice of $j_{*\mathrm{obs}}$, $j_{*\mathrm{model}}$ or $j_{*\mathrm{tot}}$. To prioritise observational data while compensating for the varying extent to which each galaxy has reliable measurements, we therefore focus on $j_{*\mathrm{tot}}$ for the remainder of this paper and refer to this simply as j_*.

To quantify the j_*–M_* relation, following previous studies we fit the expected relationship $j_* \propto M^{\alpha}$ using the form

$$\log j_* = \alpha\left(\log(M_*/M_\odot) - 11\right) + \beta \tag{2}$$

where α and β are the free parameters to be fitted.

3.1.3. Convergence of j_*

The cumulative j_* typically increases with increasing radius. If the specific angular momentum is still increasing beyond the region of the galaxy covered by the observations, the galaxy's total j_* may be higher than the value we can determine from the observed velocity map. In addition to the limitations imposed by the instrumental field of view, the distribution of star formation can be patchy and may differ from the distribution of stars, so Hα velocity measurements may not fully trace a galaxy's velocity field. To check for these biases and determine if our calculated values of j_* correspond to the total j_* of the galaxy, we calculated the cumulative value of j_* as the radial limit is increased from zero out to the edge of the field of view and looked to see if j_* converges to a constant value within the radius of our measurements.

The cumulative specific angular momentum as a function of radius for all galaxies in our sample is shown in Figure 4. In the majority of cases, j_* appears to be converging to a constant value within the limits of our observations. To check this quantitatively, we followed a similar procedure to Mancera Piña et al. (2021a), though in our case we found the cumulative j_* profiles to be well represented by an exponential function; see for example Figure 5. Taking the value of the fitted function at infinity as the j_* value each profile is converging towards ($j_{*,\infty}$), we used the ratio of the total j_* value attained within our measurements with ($j_{*,\infty}$) as a measure of how much each profile has converged. We found that 59 (85%) of our galaxies attain at least 80% of their extrapolated ($j_{*,\infty}$) value within our observational footprint.

3.2. Simulation

3.2.1. Optical images

We first check that the morphology of our simulated galaxies reproduces the observational sample they are compared to. We use the radiative transfer code SKIRT (Camps & Baes 2015) to simulate light being emitted from the stars and travelling through the galaxy interstellar medium before reaching a hypothetical VLT observatory. The galaxy is placed at a distance such that the FLAMES footprint covers 3 effective radii. We largely follow Rodriguez-Gomez et al. (2019), who created SKIRT images for higher-mass IllustrisTNG galaxies. We employ the Bruzual & Charlot (2003) Spectral Energy Distributions (SEDs) to model the emission spectrum of the stellar particles, selecting the Chabrier Initial Mass Function (Chabrier 2003). Star particles which are younger than 10 million years are considered to be star-forming regions, with a star formation rate equal to the mass of the stellar

https://doi.org/10.1017/pasa.2026.10248 Published online by Cambridge University Press

particle divided by 10 million years. The emission from these particles is modelled separately using the MAPPINGS-III SED (Groves et al. 2008), which specifically models star forming regions. Examples from the simulation sample are shown in Figure 6.

3.2.2. Mock observational maps

For the simulation sample, we first calculated the true j value separately for the star, gas, and dark matter particles within 1, 2, 3, and 5 R_e, and finally for all particles in the galaxy's halo. This was done by calculating the angular momentum of each individual particle around the centre of the galaxy and summing them to find the total angular momentum and dividing this by the total mass of all particles used in the calculation. We also determined j for the gas that was actively undergoing star formation to see how it is related to the j_* of the resulting stars. This was carried out for all 100 snapshots of the simulation (from the time when the galaxy's progenitor halo first formed stars), resulting in the full time evolution of j for each component of the galaxy.

While the simulation has the great advantage of allowing us to calculate the galaxy's true angular momentum directly, this needs to be tied back to our observations. To this end, following the methods of Deeley et al. (2021), we recreated our SHαDE observations for the simulated galaxies so that we could measure j_* in the same way as we did for the observed galaxies. This serves both as a test that our observational methods are able to recover the intrinsic j_* of the galaxy and as a test that the simulation reproduces the distribution of angular momentum that we observe. For this we use the projection of the galaxy's particles onto the x–y spatial plane (giving effectively a random projected orientation for each galaxy) and designate the z-axis as the line-of-sight direction to the observer. Firstly we fit concentric ellipses to the g-band flux distribution of the stellar particles in order to find the projected orientation of the galaxy, and hence the angle of its semi-major axis. We then overlay the FLAMES instrument footprint (consisting of 14 by 22 spaxels) onto the galaxy, angled so that its lengthwise direction is aligned with the galaxy's longest axis, and re-scale the galaxy's projected size so that the FLAMES window covers 3 times the galaxy's effective radius.

Since our observed velocities are measured using the Hα emission from star-forming gas, we use the star-forming gas particles in the simulated galaxies for the velocity calculations. IllustrisTNG does not model Hα emission directly, however Hα emission is closely related to the star formation rate, since it is the bright young stars ionising their surrounding gas that leads to this emission. We therefore use the star formation rate of each gas particle to derive its Hα emission, using the relation in Kennicutt (1998*a*). Even though this calibration assumes an IMF and solar metallicity, for our purposes here the absolute value of the Hα emission is not important. The velocities of the gas particles are then weighted by their Hα emission, and gas particles with no Hα emission (which would be invisible to our observations) are left out of the calculation.

To then calculate a line-of-sight velocity and velocity dispersion for each spaxel of the FLAMES footprint, we firstly account for the point-spread function (PSF) of the observations by creating a Gaussian function centred on that spaxel, with a full-width-half-maximum corresponding to the SHαDE average PSF of 0.88 arcsec. We then create a weighted histogram of velocities (in the z direction) using the value of that Gaussian at the location of each gas particle (in addition to the particle's Hα emission) as the weight. The central velocity of the resulting histogram

Table 1. Observational sample, with (a) galaxy SHαDE ID number; (b) stellar mass; (c) effective radius; (d) j_* calculated from the deprojected observational data; (e) j_* calculated from the model; and (f) j_* calculated from the combination of the observational data and model, where the model is used to fill in missing spaxels in the observational data. Columns (d), (e), and (f) are given in units of $\log(j/\mathrm{kpc\ km\ s^{-1}})$.

(a) ID	(b) $\log M_*/\mathrm{M}_\odot$	(c) $\mathrm{R_e}$ (kpc)	(d) $\log j_{*,\mathrm{obs}}$	(e) $\log j_{*,\mathrm{mod}}$	(f) $\log j_{*,\mathrm{tot}}$
1	7.4	0.9	0.87	1.01	1.01
2	7.6	1.6	1.12	1.73	1.73
9	7.9	2.5	1.89	2.07	2.07
42	7.9	1.2	0.69	0.73	0.74
46	7.2	0.7	0.58	0.94	0.94
55	7.3	0.6	0.09	0.56	0.56
56	7.8	1.2	0.97	1.02	1.03
59	7.3	0.7	1.36	1.67	1.68
64	6.3	0.9	0.59	0.76	0.77
128	8.1	2.4	1.66	1.87	1.88
132	6.8	0.8	0.62	0.82	0.84
136	8.0	1.1	0.8	1.02	1.02
137	7.9	1.0	1.99	2.2	2.21
148	7.8	1.0	1.28	1.88	1.88
151	8.2	1.2	1.49	1.72	1.72
152	7.5	1.9	1.55	2.13	2.14
165	7.0	0.7	0.72	1.09	1.08
171	7.5	0.9	0.83	1.09	1.1
194	7.0	1.2	0.7	0.86	0.87
200	6.4	0.4	0.59	0.64	0.63
218	7.4	1.0	1.07	1.3	1.3
231	7.8	0.6	0.87	1.37	1.37
260	5.9	0.4	0.53	0.61	0.61
271	8.3	1.4	1.81	2.07	2.08
283	8.2	1.7	0.64	0.74	0.73
284	5.8	0.6	0.26	0.65	0.64
286	7.2	0.7	-0.06	0.38	0.38
288	7.7	0.8	0.56	1.29	1.29
311	8.2	1.7	1.62	1.95	1.97
314	7.5	2.0	1.38	1.67	1.67
315	6.7	0.7	1.15	1.26	1.29
319	7.5	1.5	1.3	1.67	1.68
320	7.5	0.9	1.24	1.54	1.54
322	7.0	1.0	0.92	1.3	1.31
323	7.6	2.8	1.34	1.72	1.72
327	7.9	1.8	1.5	1.77	1.78
330	8.0	1.3	1.9	2.21	2.22
331	7.9	1.1	1.21	1.62	1.62
343	6.4	0.6	0.83	0.83	0.89
344	7.1	1.8	1.49	1.74	1.76
352	6.7	0.6	0.24	0.98	0.99
424	10.1	7.2	2.51	2.72	2.72
431	7.0	0.7	0.4	0.74	0.74
433	7.6	1.1	1.43	1.41	1.46

https://doi.org/10.1017/pasa.2026.10248 Published online by Cambridge University Press

Table 1. Continued.

(a) ID	(b) $\log M_*/M_\odot$	(c) R_e (kpc)	(d) $\log j_{*,obs}$	(e) $\log j_{*,mod}$	(f) $\log j_{*,tot}$
435	7.8	0.9	0.61	0.98	0.98
469	7.5	0.7	0.78	0.84	0.91
496	5.7	0.2	0.12	0.44	0.45
520	7.8	0.8	1.7	2.08	2.08
296934	10.2	5.0	2.64	2.98	2.96
106049	8.8	2.3	2.0	2.24	2.26
319150	8.6	1.5	0.88	1.25	1.25
511921	9.2	1.6	1.94	2.25	2.25
594906	9.8	2.4	2.62	2.7	2.73
9008500356	10.4	5.4	2.64	3.2	3.2
9011900128	9.5	3.6	2.15	2.47	2.47
9016800065	9.8	4.8	2.16	2.53	2.52
9016800314	9.9	4.5	1.95	2.72	2.72
9091700123	9.7	3.5	2.11	2.31	2.32
9091700137	10.7	6.1	2.66	2.89	2.89
9091700444	10.4	4.6	2.6	2.92	2.92
9239900178	10.6	4.6	2.08	2.7	2.7
9239900182	10.6	4.8	2.57	2.9	2.9
9239900237	10.3	5.3	2.65	2.9	2.91
9239900370	10.0	4.4	2.24	3.15	3.15
9388000269	10.5	4.2	2.52	2.92	2.91

then corresponds to the measured line-of-sight velocity, and the spread (standard deviation, σ) corresponds to the velocity dispersion. This is equivalent to measuring the central velocity and width of the Hα emission line. The same Gaussian is also used to find the weighted sum of the Hα emission in order to find the Hα flux of that spaxel, and it is used to weight the luminosities of stellar particles to determine the stellar flux. Finally, random noise is added to the velocity map in relation to the strength of the Hα emission for each spaxel.

Once we have the stellar flux, Hα emission, and line-of-sight velocity maps for each galaxy, we can then follow the same process used to find j_* for the galaxies observed by SHαDE, allowing us to make a direct comparison to the observed values and link these to the intrinsic angular momentum and evolutionary history of these galaxies. Figure 7 shows examples of the resulting Hα flux, velocity field, and modelled velocity field for three galaxies; these can be compared to the observed example shown in Figure 3.

3.2.3. Galaxy histories

We then followed the evolution of each galaxy's angular momentum, to gain insight into how this relation arises and evolves. At each snapshot in the galaxy's history, we calculate the intrinsic j_* of the star and gas particles in the same way as above (we do not derive observational-equivalent j_* values at every snapshot due to the time-intensive nature of these calculations, instead using the intrinsic j_* calculated directly from the particles). Following the same methods as Deeley et al. (2021), we use the sublink halo trees to track and record merger events, including minor mergers (with a mass ratio between the progenitor galaxies of between 1:10 and 1:3) and major mergers (with a mass ratio greater than 1:3). In doing this, we take into account pre-merger mass loss and the halo switching problem (see the above-mentioned paper for a complete description). We also track various other properties of the galaxies through their histories, including star formation rate, black hole accretion rate, effective radius, colour, and metallicity, among many others.

4. Results

4.1 Fall relation for dwarf galaxies

Figure 8 shows the specific angular momentum for the SHαDE galaxies, including both the high-mass 'control' galaxies in red and the dwarf galaxies in blue. We compare these findings with the Fall relation derived from disc galaxies by Posti et al. (2018), with $\alpha = 0.55$ and $\beta = 0.34$. The high-mass disc galaxies neatly follow the expected relation with little scatter. This illustrates that deriving j_* from these Hα emission line observations is able to recover j_* values consistent with those of previous studies of higher-mass galaxies, and in addition, shows that the angular momentum of star-forming regions is tracing the angular momentum of the general stellar population. The dwarf galaxies in our sample, while featuring a larger degree of scatter particularly for stellar masses between $10^7\ M_\odot < M_* < 10^8\ M_\odot$, follow the relation of high-mass disc galaxies extrapolated to lower masses. The j_* values for each galaxy are provided in Table 1.

Following Posti et al. (2018), we carry out a log likelihood fit to Equation (2) accounting for the uncertainties in j_* (as determined from Monte Carlo simulations, see Section 4.2) and intrinsic scatter orthogonal to the relation. We then employ the python package `emcee` (Foreman-Mackey et al. 2013) and use a Monte Carlo Markov chain to sample the posterior distribution in order to determine the posterior 1σ range. We find a best fit over the complete mass range of $\alpha = 0.53 \pm 0.04$ and $\beta = 3.23 \pm 0.11$, with an intrinsic scatter of 0.35 dex (where the uncertainties correspond to the 68 per cent credible interval). This is in close agreement with Posti et al. (2018) and shows that this relation can be extended down to stellar masses as low as $10^6\ M_*(M_\odot)$, thus covering 5 orders of magnitude in stellar mass.

Given that the maximum extent of our measurements varies across our sample, we restricted the radius to which j_* is calculated to 1, 2, and 3 effective radii in order to determine how the varying radial extent may influence our results. While the absolute j_* values across the whole sample increase as the radial limit increases and we include more of the outskirts, the observed result of a continuation in the j_*–M_* relation from high-mass to low-mass galaxies remains consistent, showing that the varying radial extent of our data does not significantly impact our conclusions.

Since our sample is selected to be star-forming, quenched dwarf galaxies may deviate or be offset from this relation (as is the case for the high-mass elliptical galaxies). As a test of whether there may be a significant difference between the populations, we look for a correlation within our sample between the star formation rate and the residuals from the fitted relation. We do indeed observe such a correlation, with dwarf galaxies above the relation tending to have higher star formation rates relative to those below (Spearman's correlation coefficient = 0.48, p-value = 0.001). Such a relationship is consistent with previous findings of a correlation between the neutral gas fraction and j (Hardwick et al. 2022), with gas-rich galaxies having higher j values. Separating

https://doi.org/10.1017/pasa.2026.10248 Published online by Cambridge University Press

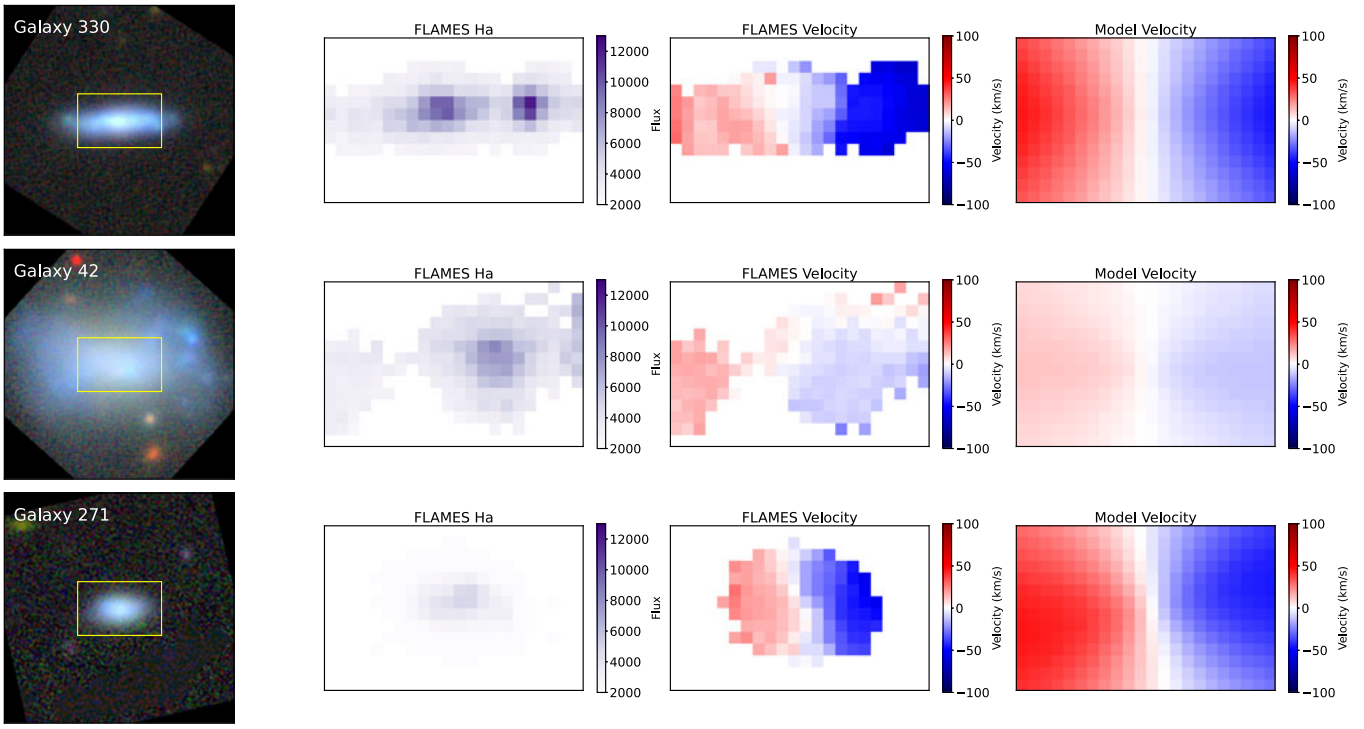


Figure 3. Examples of the SHαDE kinematic maps and the corresponding velocity field models. The left column shows optical images taken by the Dark Energy Legacy Survey, with the FLAMES footprint shown by the yellow box. The second and third columns display the Hα emission and the Hα-derived velocity map, respectively, and the final column shows the velocity field produced by the best-fitting rotating-disc model of the galaxy.

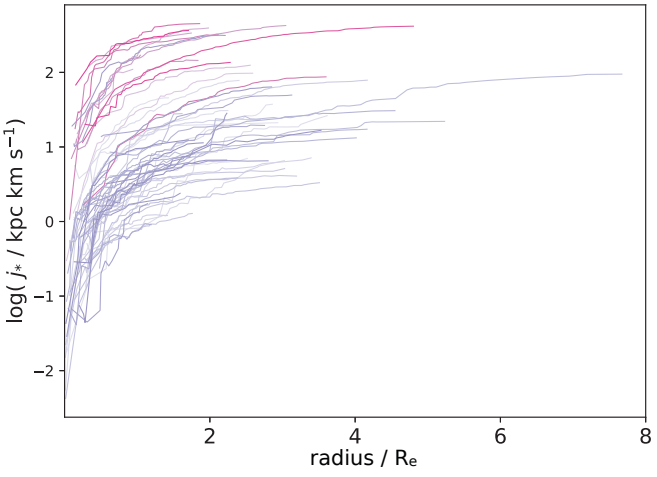


Figure 4. $j_*(< r/R_e)$ as a function of radius for the dwarf (blue) and control (red) galaxies. The radial profiles approach a constant value towards the edge of our observed limits in most cases, showing that our observations extend far enough over the galaxies to capture the bulk of their total angular momentum.

our sample into two populations above and below the median specific star formation rate $\log(\mathrm{sSFR/yr^{-1}}) = -9.45$ and carrying out a log likelihood fit on each population, we find $\alpha = 0.56 \pm 0.07$, $\beta = 3.46 \pm 0.25$ for the population with higher star formation rates and $\alpha = 0.59 \pm 0.06$ and $\beta = 3.22 \pm 0.17$ for the population with lower star formation rates. While the normalisation of the relation is shifted to higher values for galaxies with higher star formation rates, the slopes are consistent with each other and both are consistent with the complete sample, within uncertainties. This suggests that our sample selection biases the normalisation but not necessarily the slope, however a quenched dwarf galaxy sample is needed to fully test this finding. We therefore emphasise that our results apply primarily to the star-forming dwarf galaxies, with additional observations being needed to study the quenched population.

Figure 9 shows the sample categorised by visual morphology; those that resembled discs are shown in Figure 9(a), compact galaxies in Figure 9(b), and clumpy irregular galaxies in Figure 9(c). Disc galaxies follow the global j_*–M_* relation with a smaller degree of scatter (median offset $= 0.035$, $\sigma = 0.30$) relative to the compact (median offset $= 0.002$, $\sigma = 0.42$) and irregular (median offset $= 0.003$, $\sigma = 0.43$) galaxies. Restricting to disc galaxies below $10^{8.5}$ $M_*(\mathrm{M}_\odot)$, the median offset becomes 0.093 with $\sigma = 0.35$. Together, these results show that despite the more disordered structure of irregular galaxies and the lack of a clear disc in compact galaxies, these galaxy types continue to follow the j_*–M_* relation to below 10^6 $M_*(\mathrm{M}_\odot)$, albeit with increased scatter.

4.2. Monte Carlo model fitting

To better characterise the uncertainties in our calculations of j_*, we performed a Monte Carlo simulation of our observations. For each galaxy, we created 100 random realisations where the velocity maps, mass, and redshift were all randomly altered based on the measurement uncertainties in each respective property. For the velocity maps, the velocity value of each individual spaxel was replaced by a random number from a normal distribution centred on the observed value and with standard deviation equal to the uncertainty in the measurement for that spaxel. The redshift and mass of the galaxy was likewise replaced by a random

https://doi.org/10.1017/pasa.2026.10248 Published online by Cambridge University Press

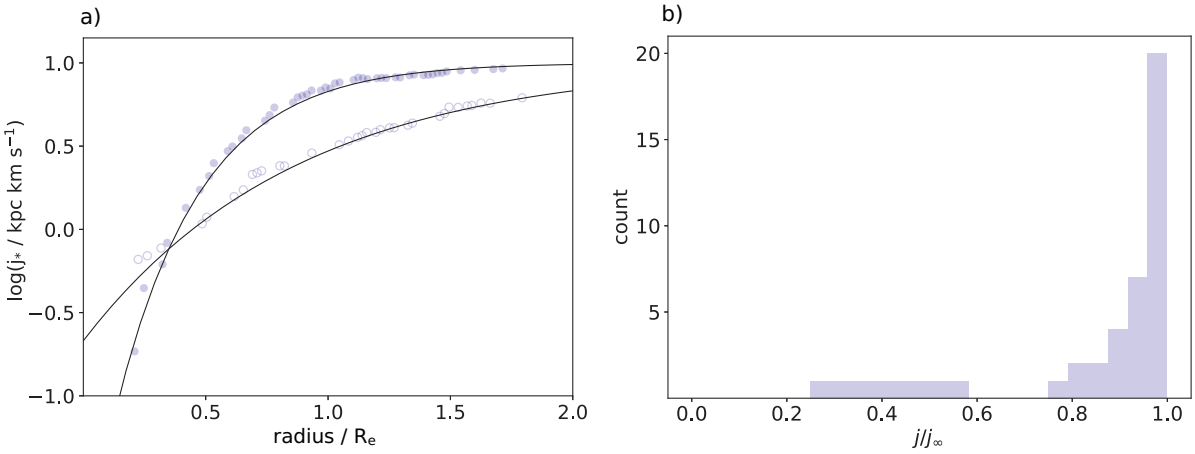


Figure 5. Convergence of the cumulative $j_*(<r/R_e)$–R profiles for our observational sample. (a) displays the cumulative j_* profile for a converging (ID: 1, filled points) and non-converging (ID: 322, open points) galaxy, along with their respective best-fit exponential curve. The exponential function provides a good description of the profile and demonstrates how well each profile has converged on the total j_* value. (b) shows the distribution of $j_{*,\max}/j_{*,\infty}$, illustrating that the majority of our galaxies are approaching convergence.

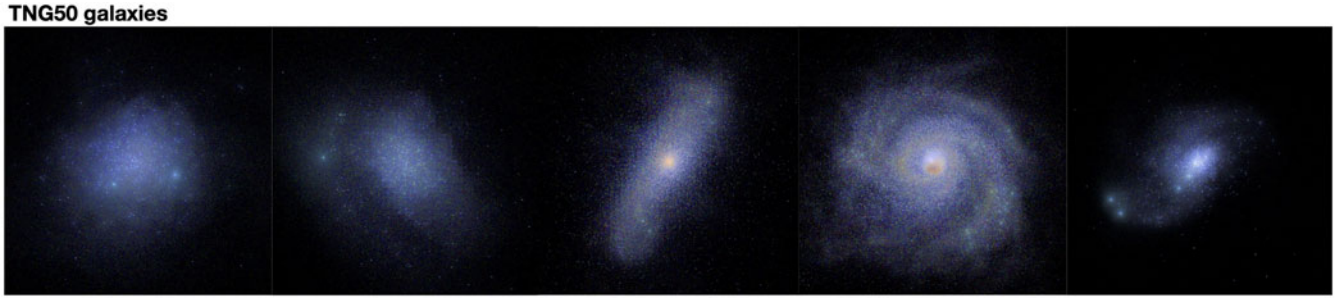


Figure 6. Optical images of example simulated dwarf and low-mass spiral galaxies created using the radiative transfer code SKIRT. The images demonstrate the range of morphologies in the simulated galaxies, which resemble the variety of morphologies in our observational sample (see Figure 1).

number taken from a normal distribution centred on the original measurement and with the appropriate standard deviation.

The resulting 100 realisations were then analysed in the same way as the original observations, including the fitting of a disc model and the subsequent calculation of j_* from the deprojected maps. The distributions of j_* from this process are displayed in Figure 10. There is great variety in the shapes and sizes of the resulting distributions. Many highly disc-like galaxies have a very small range of j_* values, showing that in these cases the resulting disc model is very consistent between different realisations, and hence that it is robust. In other cases there is a large range of j_* values, often for more irregular galaxies, showing that there is greater uncertainty in the modelling of these galaxies and reflecting the fact that it is difficult to model them with a disc. There are also cases where there are two favoured solutions in the model fitting, creating two regions in the j_*–M_* plane; an example of this is shown in Figure 10(b). In this case the higher-j_* realisations occur when the galaxy is modelled as being closer to face-on, meaning that its intrinsic rotational velocity has to be higher in order to match the value observed along the line-of-sight.

4.3. Testing the thin-disc assumption

As dwarf galaxies often have an irregular or thick-disc morphology, the method of deprojecting a thin kinematic disc, as used here, may not lead to realistic modelling of their intrinsic kinematics. We therefore test an alternative method for deprojecting the line-of-sight velocities for each dwarf galaxy based on the optically observed ellipticity (derived from multi-Gaussian fitting to SDSS imaging, see Barat et al. 2020) and systematically varying the assumed intrinsic disc thickness (q_0) from 0 to 0.35. For higher q_0 values, our sample size becomes too small to carry out a meaningful fit due to the loss of galaxies (such as nearly edge-on discs) which cannot physically have a q_0 value at the set quantity. Using these deprojections, we then calculated j_* as before. For low values of q_0, we found close agreement between the two methods (for $q_0 = 0.05$: median offset $= -0.044$, $\sigma = 0.062$ dex), showing consistency between the optically-derived and kinematically-derived disc deprojections. For each value of q_0 we fitted Equation (2) for α and β to the resulting j_*–M_* plane using the same method as before, and compared it to our original result for the dwarf galaxy population. We found these relations with varying q_0 to be consistent with our original result for the dwarf galaxies ($M_* \leq 10^{8.5}$ $M_\odot$) within uncertainties. This suggests that for the sample presented here, our derived slope remains consistent when varying the assumed disc thickness up to $q_0 = 0.35$.

4.4. Comparison with SAMI and the effect of the PSF

Since the 20 control galaxies in our sample were taken from the SAMI survey, we can also use the SAMI velocity maps as an observationally independent way to measure their angular

https://doi.org/10.1017/pasa.2026.10248 Published online by Cambridge University Press

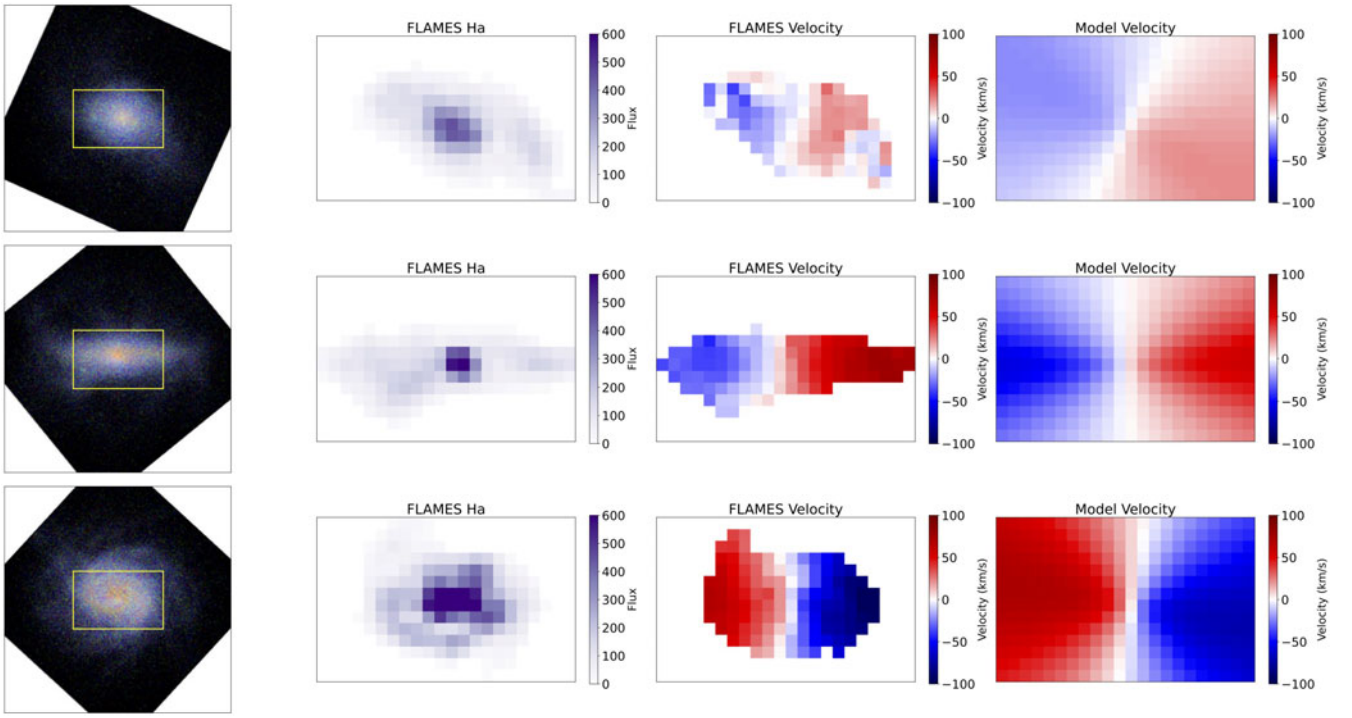


Figure 7. Examples of observationally-equivalent flux and kinematic maps for the simulated galaxies. The maps were made to mimic the SHαDE survey, showing the Hα flux and line-of-sight velocity over a 14 × 22 spaxel window resembling the FLAMES footprint. These maps were then analysed using the same methods as for the observational sample, resulting in the modelled kinematic maps shown in the right-hand column. The optical images on the left-hand side were created using the radiative transfer code SKIRT.

momentum. The SAMI survey derived velocity maps from both their stellar component (using the stellar absorption lines) and from their ionised gas component (measured from the gas emission lines). With Hα emission being a component of the gas emission, we expect the gas velocity field to more closely match what was observed in SHαDE. We found that the angular momentum measured from the SAMI velocity maps was consistently lower than SHαDE for both the stellar and gas component, and with the SAMI stellar component being lower than the SAMI gas component in most cases. To test whether this may be due to the different field of views of the two instruments, we overlaid the Argus footprint onto the SAMI maps, with its position and orientation matched to the SHαDE observation. The resulting j_*–M_* relation was tighter and more consistent with the SHαDE relation, however the downward offset remained. This is likely due to the SAMI survey having a larger PSF (median full width at half-maximum (FWHM) of 2.04 arcsec, Croom et al. 2021) relative to the SHαDE survey (median FWHM of 0.88 arcsec). The larger PSF acts to blur the velocity field, reducing the velocity gradient across the field and therefore reducing its apparent rotation (while increasing the apparent velocity dispersion).

To determine how the PSF of our observations may influence the derived j_*–M_* relation, we tested for a correlation in the scatter of the j_*–M_* relation with both the number of resolved elements in each galaxy and with their effective radii as measured in arcseconds on the sky. In relation to the number of resolved elements, we found no significant trend with the scatter from the relation (Spearman's correlation p-value = 0.48). We do however find a weak but significant trend between the scatter and effective radius in arcseconds (Spearman's correlation coefficient = −0.11, p-value = 0.026). This is in the opposite sense to what one may expect from PSF blurring, and may reflect the increased reliance on model extrapolation to 3 effective radii.

4.5. Model Fall relation

We then attempted to reproduce the Fall relation using our sample of galaxies from the IllustrisTNG-50 simulation. To be consistent with our observational sample, j_* was calculated from the velocity maps made to resemble the SHαDE observations (deriving the maps from the Hα emitting gas); the resulting relation is shown in Figure 11, along with the SHαDE observations from Figure 8. Above a stellar mass of 10^9 $M_*(\mathrm{M}_\odot)$, the simulated galaxies closely follow the relation found by Posti et al. (2018), and are in good agreement with the high-mass SHαDE control sample. This agreement of IllustrisTNG with previous observational studies in this mass range has been seen previously by Genel et al. (2015) (who used the original Illustris simulation), and Rodriguez-Gomez et al. (2022), Du et al. (2022) and Hardwick et al. (2023) (all using IllustrisTNG). However, all of these studies were restricted to masses above 10^9 $M_*(\mathrm{M}_\odot)$. Below this mass there is an increased scatter towards lower j_* values, with the upper edge continuing to follow the observed relation. Alternatively this could be seen as a drop and flattening of the relation, as reflected in the residual plot in the bottom panel of Figure 11. The low-j_* dwarf galaxies may be missing from our observational sample if they are faint or have low surface brightness, or if they reside in higher-density environments not probed by our nearby dwarf galaxy sample.

We compared our derived j_* values to the intrinsic values of the galaxies as calculated from their particles directly. We found relatively close agreement in j_* between our observation-equivalent values and the star-forming particles, with the residuals

https://doi.org/10.1017/pasa.2026.10248 Published online by Cambridge University Press

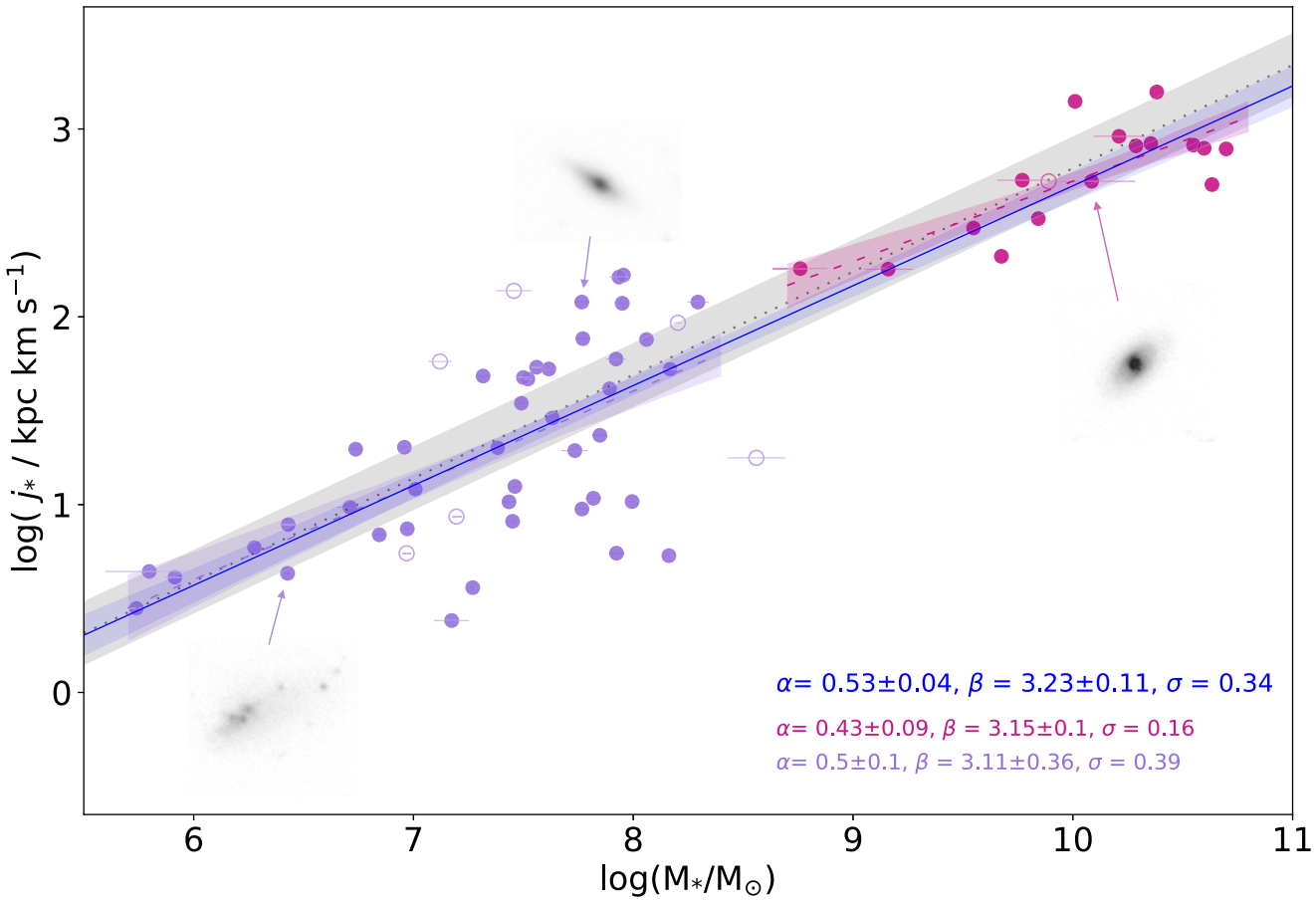


Figure 8. The j_*–M_* relation for our observational sample, showing the SAMI control galaxies (magenta) and the dwarf galaxies (purple). The dark blue line and associated shaded region display the fit of the entire sample to Equation (2) along with its 68% credible interval. Fits for above and below $10^{8.5}$ M_*(M$_\odot$) (corresponding to the control and dwarf galaxy samples) are shown by the dashed purple and magenta lines, respectively. The corresponding values and intrinsic orthogonal scatter (σ) for all three fits are given in the bottom right of the figure. The black dotted line and associated grey shaded region display the relation found by Posti et al. (2018). Non-converging galaxies ($j_{*\mathrm{tot}} < 0.8j_\infty$) are shown with an open circle. Example HSC *r*-band images of a large disc galaxy, a small disc galaxy, and an irregular dwarf galaxy are shown. The control galaxies closely follow the relation found by Posti et al. (2018), and our dwarf sample extends this relation down to below 10^6 M_*(M$_\odot$).

(observed − intrinsic) having a median bias of 0.08 and a scatter (one standard deviation) of 0.39. We found our observed values to overestimate the intrinsic stellar j (median bias = 0.44, scatter = 0.43), highlighting that the star-forming component has elevated angular momentum relative to the broader stellar component. We also find the relation between our observed values and the intrinsic j_* to deviate from a one-to-one relation, finding a gradient m of 0.80 ± 0.02 for $j_{\mathrm{observed}} = mj_{\mathrm{intrinsic}}$, largely driven by an increase in scatter in the intrinsic stellar j at low mass. This suggests the difference in j between the star-forming component and stellar component may be greater for dwarf galaxies relative to high-mass galaxies, though again we stress the potential resolution limitations of the simulation at lower masses.

In the process of calculating the intrinsic angular momentum, we found the total angular momentum vector of all stellar particles within each galaxy, allowing us to determine the inclination angle as projected onto the observed x–y plane. We found no significant correlation between the inclination angle and the residuals of the observed − intrinsic j (Spearman's coefficient = 0.01, p-value = 0.76), implying minimal bias in our observed values due to inclination. As a kinematic measure of the disc thickness, we calculated a simplified intrinsic v/σ value (where σ is the velocity dispersion) by taking the ratio of the sum of particle velocity components within the plane of rotation to the sum of velocity components outside this plane, and found there to be no significant correlation with the residuals (Spearman's coefficient = −0.02, p-value = 0.62) We also find no significant correlation with effective radius (Spearman's coefficient = −0.06, p-value = 0.24). However as stated through this paper, when applying these findings to our observational results, potential resolution effects within the simulation should be kept in mind.

The decrease in j_* for low-mass galaxies, and the apparent flattening of the relation below 10^8 M_*(M$_\odot$) may also be a result of the simulation's limited resolution. Galaxies with stellar masses around 10^8 M_*(M$_\odot$) consist of a few thousand stellar particles, while 10^7 M_*(M$_\odot$) consist only of a few hundred stellar particles, meaning the galaxies' structures are less resolved which may lead to the loss of coherent motions. Similarly in the mass-radius relation, as discussed above, there is a flattening below 10^8 M_*(M$_\odot$). As a test of whether the observed low j_* values among the dwarf galaxies are due to resolution effects, we carried out the same analysis using the lower-resolution TNG100 and TNG300 simulations. While an increasing degree of scatter is seen as we go from TNG50 to TNG300, the distribution of galaxies on the j_*–M_* plot remains

https://doi.org/10.1017/pasa.2026.10248 Published online by Cambridge University Press

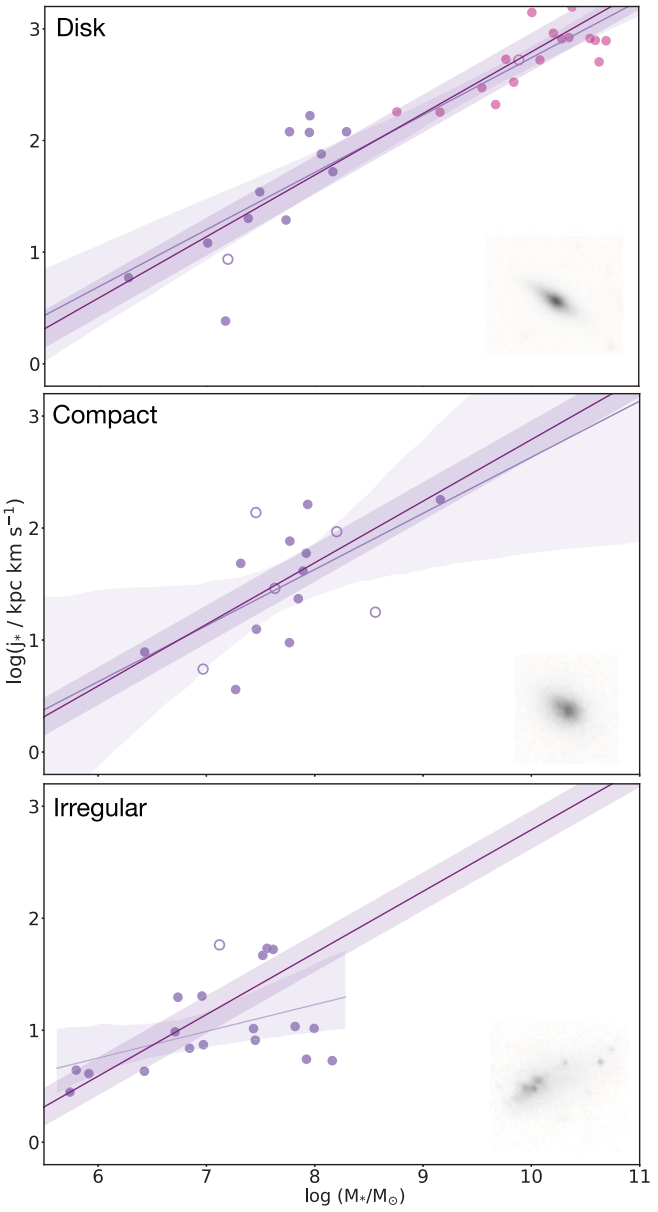


Figure 9. The j_*–M_* relation with galaxies divided by their visually classified morphology, illustrating how the deviation from the previous relationship is morphology-dependent. The top panel shows disc galaxies, the middle panel shows compact galaxies and the lower panel shows clumpy and irregular galaxies.

consistent. In particular, we do not see a change in the mass at which galaxies begin to scatter below the expected relationship – if this was purely a resolution effect, we may expect to see the downward scatter in j_* begin at higher galaxy masses as the simulation's resolution decreases. This suggests that the measured j_* seen among the dwarfs may be due to physical processes within the simulation rather than the limited resolution. We also note that the Hα kinematic maps for dwarf galaxies around 10^6 $M_*(\mathrm{M}_\odot)$ remain physical, with coherent rotation clearly visible in well-ordered systems.

4.6. Evolution of j_*

Figure 12 displays the evolution of the specific angular momentum for a sample of galaxies in our simulation sample. The evolution is plotted in the j_*–M_* plane, showing the stellar mass and specific angular momentum at each simulation snapshot for every galaxy. Considering the computational burden of generating mock observations, here we use the true j_* calculated from the individual particles in each galaxy. The particles used here are the gas particles weighted by their star formation rate, in order to match the Hα component measured in our observation sample. The combined evolution of all galaxies forms a flat distribution at the low-mass end, a large dip to low angular momentum around $10^7 - 10^{8.5}$ $M_*(\mathrm{M}_\odot)$ and an upward slope at higher masses. Galaxies initially form with low masses and with a relatively significant and highly fluctuating amount of angular momentum, creating the broad low-mass arm of the plot. As they grow in mass, most galaxies either fluctuate around a relatively constant value or lose angular momentum, creating the downward dip with increasing mass. At around $10^7 - 10^8$ $M_*(\mathrm{M}_\odot)$ there is a transition to a rising relation between j_* and M_*, where the galaxies appear to be gaining angular momentum as their mass further increases. This creates the upward-sloping right-hand side of the figure. From this pattern, it appears that galaxies first lose angular momentum and then either maintain or begin gaining angular momentum once they grow past a certain mass range. We note that here we are only considering star-forming galaxies, leaving out quenched elliptical galaxies which likely have differing histories. In contrast, lower-mass galaxies appear to always be losing angular momentum while gaining mass and never reach this transition point. Finally, a few galaxies are seen to dip down in j_* and to move to the left, suggesting that they are being stripped of their outer rotating disc.

Evidently, despite the apparent simplicity and tightness of the Fall relation as observed in this and various other studies in the present day, particularly for higher masses, the evolution of j_* leading up to the present-day values is very complex and dynamic. We emphasise here that we are looking at galaxies which are selected as star-forming disc galaxies at the present day; high-mass galaxies which undergo more disruptive mergers and evolve into dispersion-dominated ellipticals would experience different evolutionary histories in j_* and fall below the j_*–M_* relation at the present day.

Figure 13 displays the same information as in Figure 12, but instead we are plotting j_* as a function of time for each galaxy. The galaxy sample is divided into those which have a final mass below 10^8 $M_*(\mathrm{M}_\odot)$ and above 10^9 $M_*(\mathrm{M}_\odot)$. This more clearly illustrates that there appears to be two main evolutionary paths for the angular momentum of these galaxies, though we note that there is a continuum between these paths rather than a clear separation.

Galaxies with final masses below 10^8 $M_*(\mathrm{M}_\odot)$ initially form with higher j_*, then experience a steady loss of j_* with the passage of time. Galaxies with final masses above 10^9 $M_*(\mathrm{M}_\odot)$ also experience an initial loss of angular momentum, then in many cases undergo a rapid transition or jump to a state of higher angular momentum. The fluctuations in j_* also decrease significantly after this transition, and once it is completed the galaxies are able to maintain a very steady value of j_*, resulting in a relatively constant mean and dispersion in j_* through time for this group. Most of these galaxies have entered a steady state by 6 Gyrs after the Big Bang (corresponding to a redshift of 1), which is consistent with the lack of significant evolution in the j_*–M_* relation in observations over this redshift range for high-mass galaxies. The jump up to higher j_* does not occur at a particular critical mass; rather, it occurs once the galaxy has grown into the stellar mass range between 10^8 and 10^9 $M_*(\mathrm{M}_\odot)$. Galaxies that never reach this mass

https://doi.org/10.1017/pasa.2026.10248 Published online by Cambridge University Press

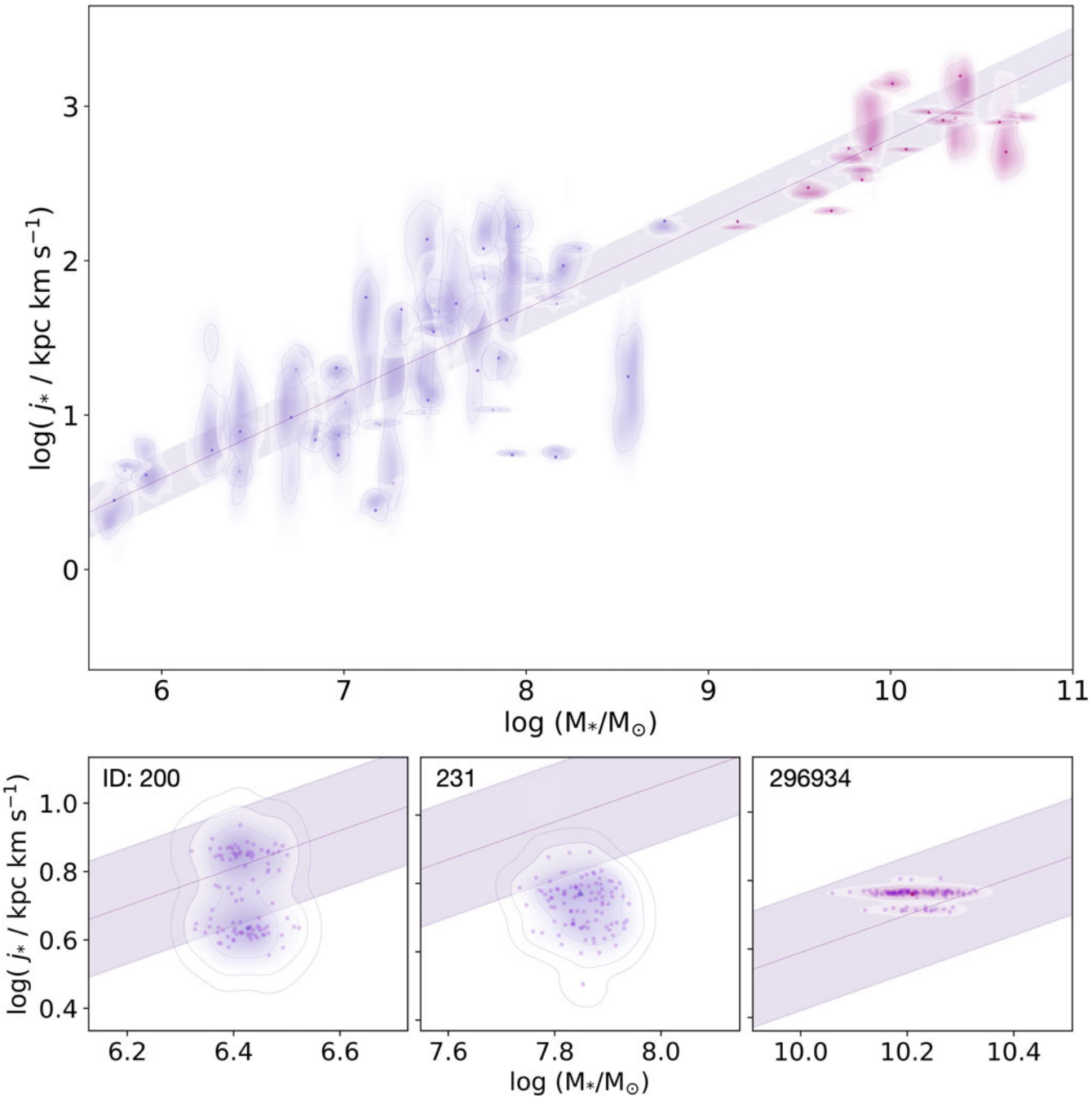


Figure 10. Distributions in j_* after 100 Monte Carlo simulations for each galaxy. The top panel shows the MC distributions of each galaxy plotted together on the j_*–M_* relation, with the colours as before; contours show 1 and 2 σ from the centre of each distribution. The lower panels show example galaxies: left – a galaxy where the MC simulations led to a bimodal distribution in j_*; middle – a more typical dwarf galaxy; and right – a typical high-mass disc galaxy.

never experience this transition, and so continue to lose angular momentum. However, as time goes on galaxies of lower and lower mass experience this jump in j_*, and so perhaps some lower-mass galaxies haven't yet had enough time to experience this transition.

It remains possible that this transition in j_* corresponds to a resolution effect, for example, the crossing of a threshold in the number of particles within the galaxy resulting in an alteration of internal dynamics. As a test on whether the jump in j_* is a result of resolution limitations, we trace the evolution of j_* for high-mass galaxies within the lower-resolution TNG100 simulation and find similar behaviour, with a transition to a high-j_* disc-dominated galaxy occurring from 10^8–10^9 $M_*(M_\odot)$; an example from TNG100 is provided in Figure A1 in the Appendix. This consistency in the j_* transition between TNG50 and TNG100 suggests that this may not be due to resolution limitations. We note also that within TNG50, the timing of this transition does not correspond to galaxies reaching a particular particle number as they grow in mass.

https://doi.org/10.1017/pasa.2026.10248 Published online by Cambridge University Press

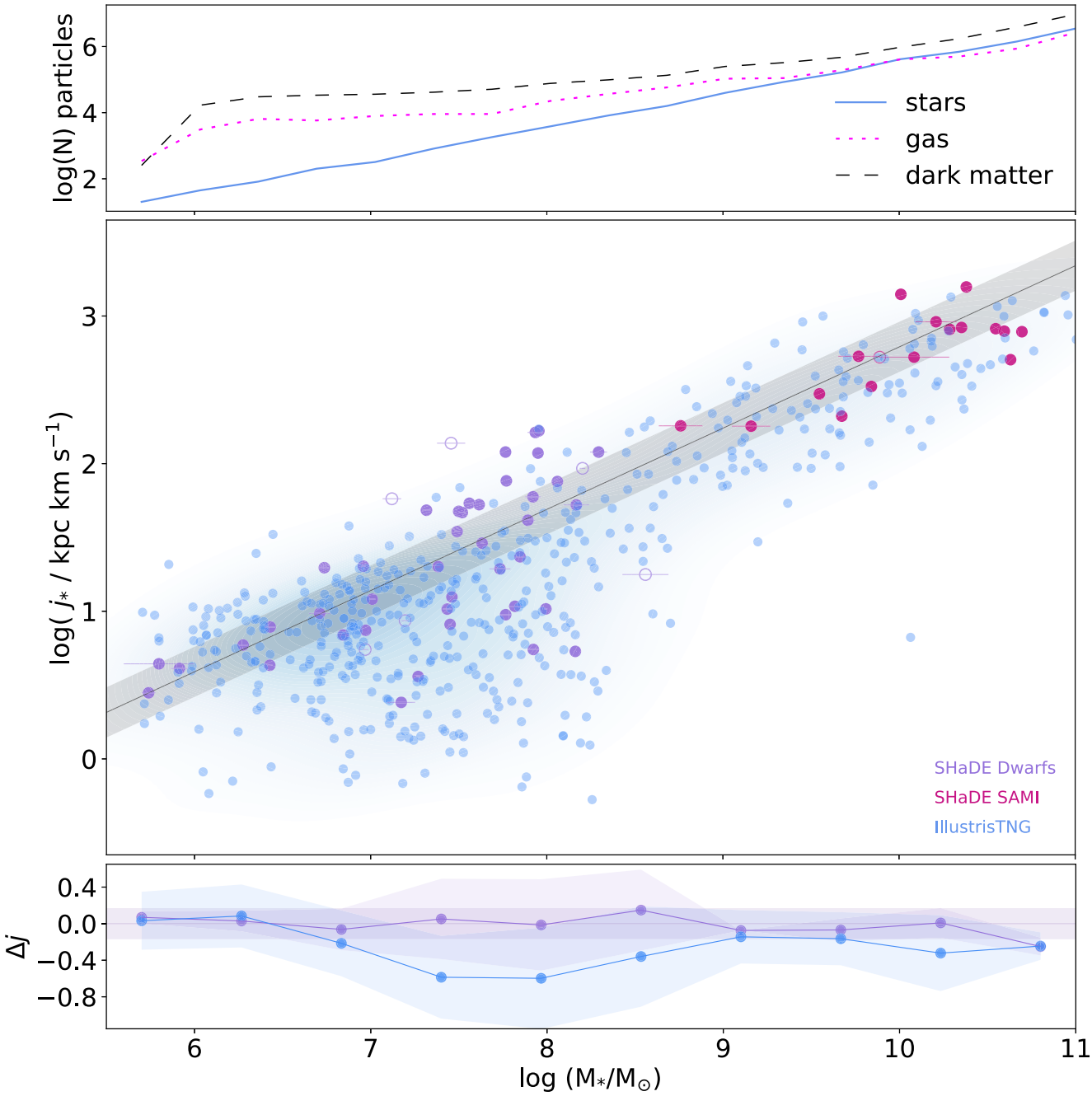


Figure 11. Comparing the j_*–M_* relation for our observational sample with that from the IllustrisTNG sample. The central panel shows the same observational data points as Figure 8, with the simulation sample added as the blue points. The distribution of the simulated galaxies closely matches the observed galaxies, including the agreement with Posti et al. (2018) at higher masses and the extension to lower values of j_* at lower masses. However the simulated galaxies have a greater range of j_* values than the observed sample, with the lower-mass dwarf galaxies having an increased scatter towards lower j_*. This is highlighted in the bottom panel, which shows the median difference between j_* and the expected relation from Posti et al. (2018) within mass bins centred on each point. The shaded regions show the standard error about each point. As an indication of how well resolved the simulated galaxies are, particularly for the low-mass end, the top panel displays the average particle number for each galaxy subhalo as a function of mass. The number of stellar particles decreases below 100 at around $10^{6.2}$ $M_*(\mathrm{M}_\odot)$ while the number of gas particles is more than 1 000 over the whole observed mass range.

To determine how the Fall relation evolves over time within our simulation sample, we performed a fit of Equation (2) for each snapshot over the complete sample and for galaxies above and below 10^9 $M_*(\mathrm{M}_\odot)$. The evolution of α and β over time is displayed in Figure 14. We find that despite the varied behaviour of individual galaxies, the value of α over the full sample reaches the present-day value at around $z = 1.5$ and becomes stable by $z = 0.6$.

4.6.1. *Transition in j_* and disc formation*

To illustrate the dynamical changes relating to the increase in j_* we compare individual galaxies which do or do not experience this transition. Figure 15 shows two such galaxies. The first example (on the left side of the figure) is a disc galaxy with a final stellar mass of $10^{8.8}$ $M_*(\mathrm{M}_\odot)$ and the second is a dwarf galaxy with a final

https://doi.org/10.1017/pasa.2026.10248 Published online by Cambridge University Press

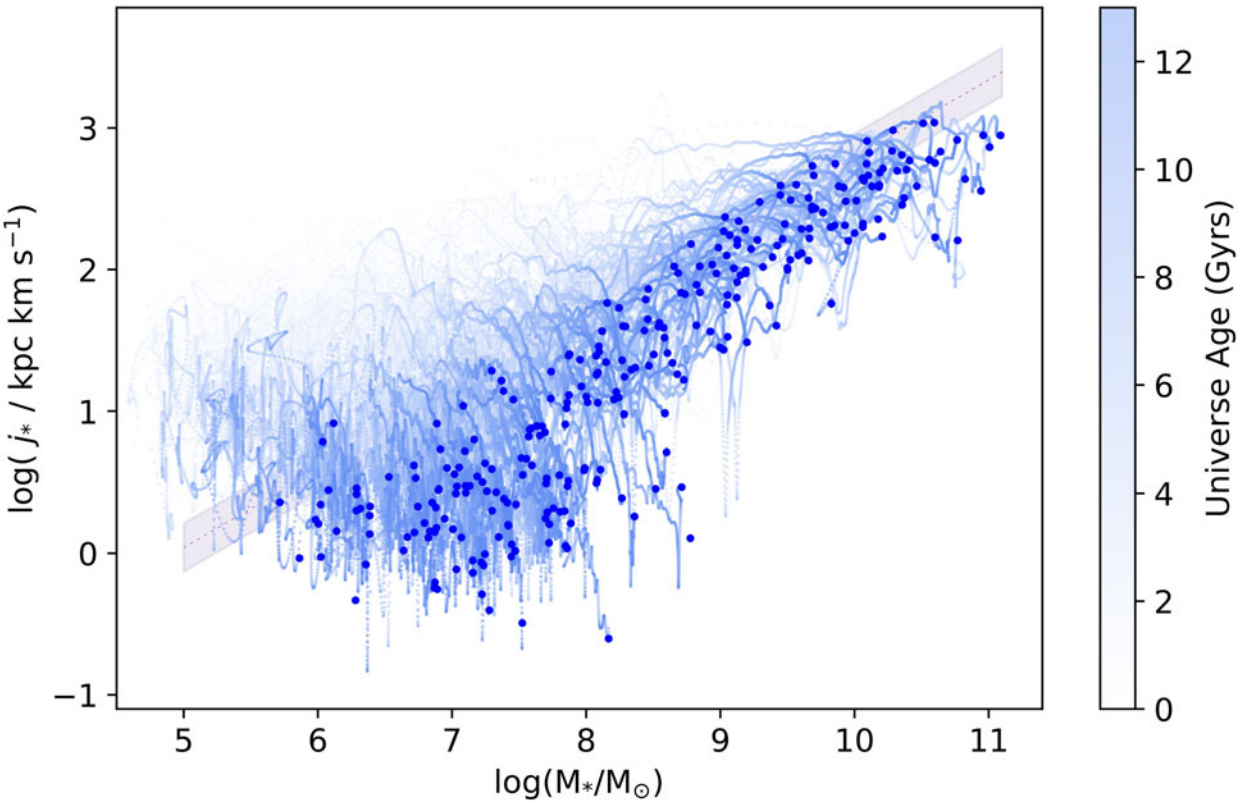


Figure 12. The j_*–M_* relation for IllustrisTNG galaxies over their evolutionary history. To reduce clutter, we only show a random sub-sample. The mass and j_* of each galaxy at every snapshot in the simulation is shown by a point, coloured by the time of that snapshot. The final positions of each galaxy are shown by the blue points. Galaxies initially forming with low masses gradually increase in mass and lose angular momentum; then, while some continue to lose momentum, others experience an increase in momentum as they continue to increase in mass.

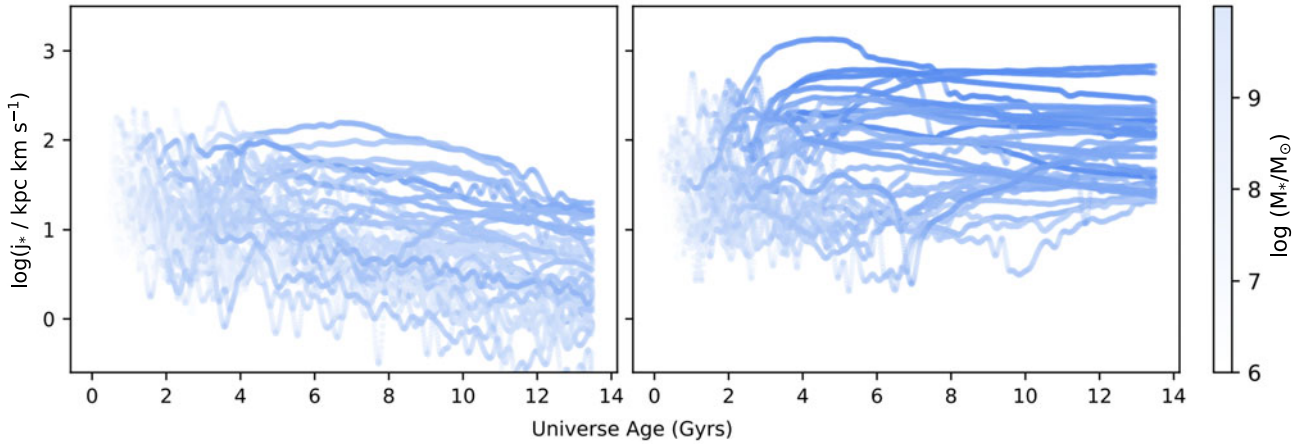


Figure 13. Evolution of j_* as a function of time for all galaxies, divided into those with a final mass below 10^8 $M_*(M_\odot)$ on the left and above 10^9 $M_*(M_\odot)$ on the right. The low-j_* galaxies, after an initial rapid decrease in j_*, continue to lose angular momentum at a steady rate, with high fluctuations in j_* for each individual galaxy. The high-j_* galaxies, meanwhile, go through the same initial loss of angular momentum before experiencing a rapid increase, eventually reaching a steady higher-j_* state.

mass of 10^7 $M_*(M_\odot)$. These two galaxies initially follow similar behaviour in their evolution of angular momentum, starting with a relatively high j_* which gradually decreases with time. The stellar and gas distributions show that at this early stage both galaxies are irregular, disordered systems with no signs of any disc components, with the gas component appearing clumpy and turbulent. However, the j_* evolution of the two galaxies diverge at around 6.2 Gyrs, when the higher-mass galaxy begins experiencing a rapid increase. This is associated with the gas beginning to collapse into a plane of common rotation, which appears nearly edge-on in this orientation. Once the galaxy settles into a new dynamical state with $\log(j_*) \approx 1.55$, the gas is now in a tight disc, and with new

https://doi.org/10.1017/pasa.2026.10248 Published online by Cambridge University Press

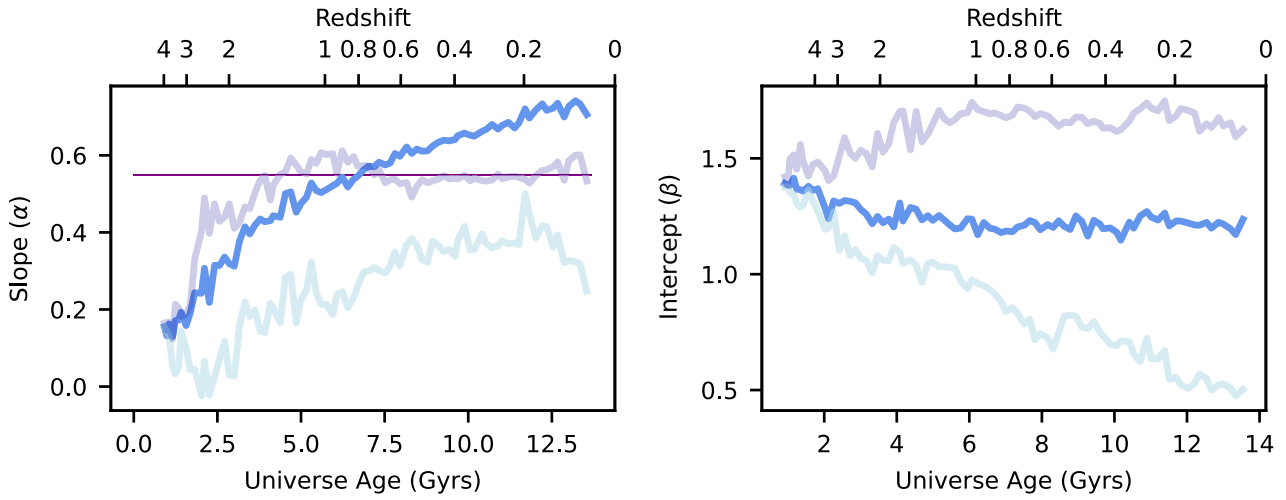


Figure 14. Evolution of the j_*–M_* relation with the age of the Universe. The left panel shows the slope of the relation while the right panel shows the intercept. Light blue lines show the evolution of galaxies which have a final mass below 10^9 $M_*(M_\odot)$, the dark blue lines shows the evolution of those which masses above 10^9 $M_*(M_\odot)$ and the purple line shows the evolution for the complete sample. The overall slope is shallower at high redshifts and increases with time until it reaches the present-day value at a redshift of around 1.5, and becomes stable by $z = 0.6$. The slope amongst the high-mass galaxies is seen to continually increase with time, while the slope amongst the dwarfs increases at a slower rate before decreasing towards the present day.

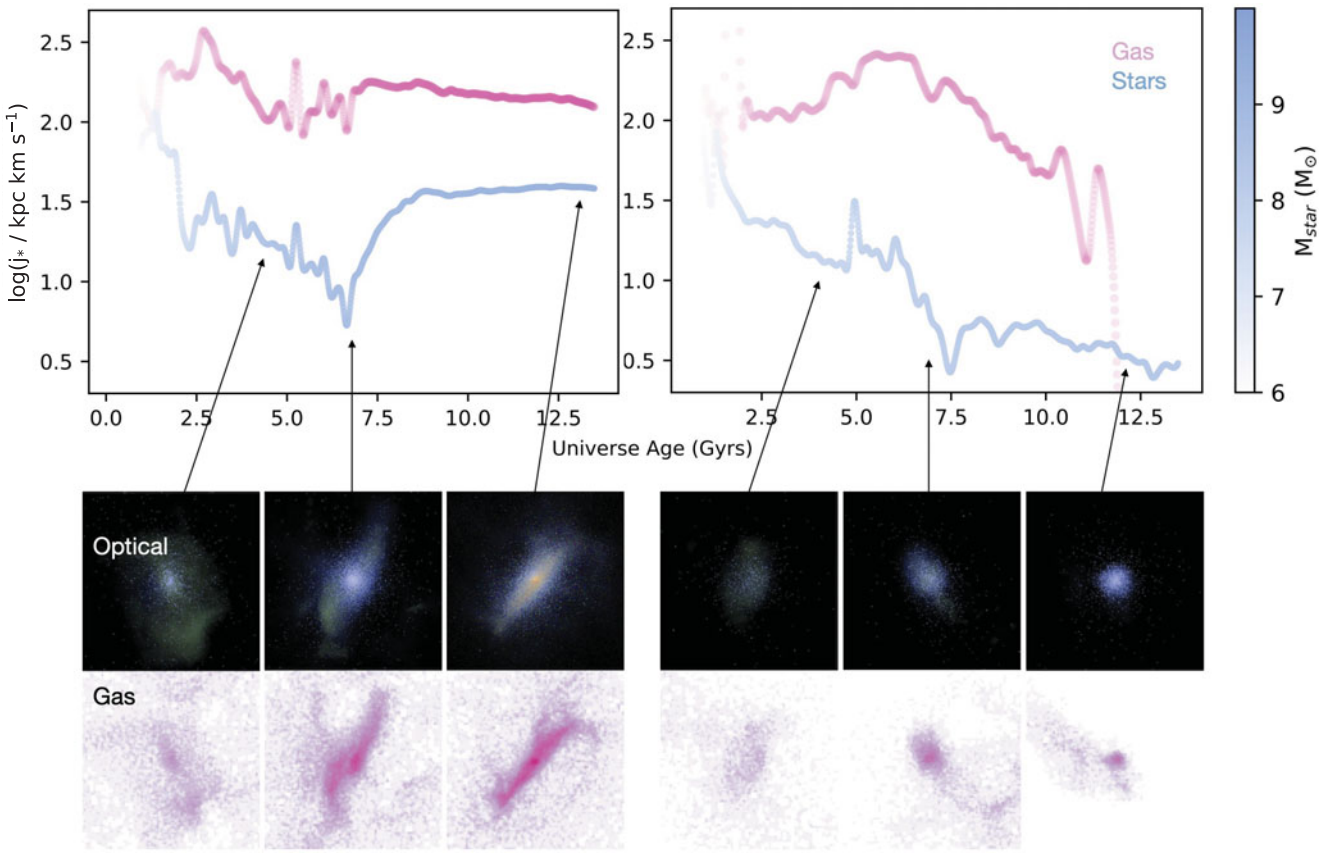


Figure 15. Examples of a galaxy with a low final value of j_* (right) and with a high final value (left). The top panels show the evolution of j_* with time, with the blue sequence showing the stellar component and the pink sequence showing the gas component. The bottom two rows show the optical image as modelled by SKIRT (top row) and the distribution of the gas component (bottom row) at three different times.

https://doi.org/10.1017/pasa.2026.10248 Published online by Cambridge University Press

stars now forming within this disc, a disc component is also clearly evident in the stars. In the case of the lower-mass dwarf galaxy, as j_* continues to decrease, the gas remains turbulent and the stellar distribution remains irregular or elliptical with no signs of a developing disc.

5. Discussion

5.1. Comparison with previous HI studies

As mentioned in the introduction, most previous studies of the specific angular momentum within dwarf galaxies have been carried out using HI observations. Our observational results are consistent with Elson (2017), in that they found their dwarf galaxies to follow the same relation as that determined for the same component in high-mass disc galaxies (in their case HI). The main difference for our study, aside from measuring a different component and finding a consistent result, is the extension of this continuation down to galaxy masses of $10^{5.7}$ $M_*(\mathrm{M}_\odot)$.

However, like Elson (2017), our results are in tension with the earlier studies by Butler et al. (2017), Chowdhury & Chengalur (2017) and Kurapati et al. (2018) who found higher values of j for the dwarf galaxy population. Elson (2017) argue that this difference, at least in the case of Butler et al. (2017), is due to the extrapolation of the HI rotation curve to radii beyond that where the rotation curve is well constrained. Chowdhury & Chengalur (2017) included a more limited sample of five dwarf galaxies, which were additionally selected to be gas-rich dwarf galaxies with a HI to stellar mass ratio greater than eight. We note that, as found by Hardwick et al. (2022), j increases with HI fraction for a given mass, and so it may be possible that this selection led to a sample of dwarf galaxies with higher-than-average angular momentum. Kurapati et al. (2018) calculated j for 11 dwarf galaxies residing in the void. Such dwarfs, as they have noted, have also been found to have higher HI gas fractions, and so it is possible that they have selected dwarf galaxies which have a higher degree of angular momentum. They noted that their results are consistent with the non-void galaxies studied in Butler et al. (2017) and Chowdhury & Chengalur (2017); however, as noted above, the dwarfs in Chowdhury & Chengalur (2017) were selected for high HI fractions and Butler et al. (2017) may have measured higher j values for other reasons.

To further investigate the compatibility of our results with previous HI studies, we looked to use our simulation sample to determine how the angular momentum of the HI and stellar components relate to each other. IllustrisTNG models the fraction of neutral gas within each gas cell, however the differentiation of neutral hydrogen into atomic and molecular states isn't directly modelled. A full treatment would require detailed post-processing of the simulation data (see e.g. Diemer et al. 2018), which we leave for future consideration. As an initial indication of potential differences between our studies, here we make a simplification by considering the fact that the mass fraction of molecular to HI gas in dwarf galaxies is typically less than 10% (Boselli et al. 2014) and measure j for the entire neutral gas component. We do this by calculating j for the gas particles weighted by their neutral gas fractions; the resulting j values for this component, along with the j values for all gas particles which are star forming, are displayed in Figure 16. The two components have similar j values for the higher-mass galaxies, however below 10^8 $M_*(\mathrm{M}_\odot)$ the neutral gas component is seen to have higher j values relative to the star-forming gas. This is an indication that measuring j from the neutral gas component may lead to higher measured values of j relative to the stellar component.

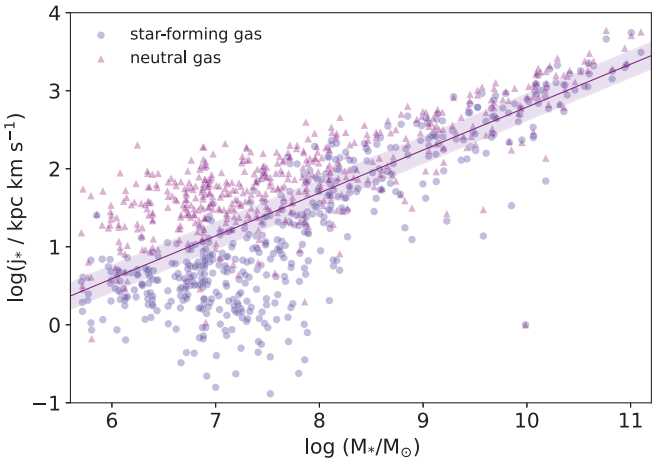


Figure 16. Comparison of the intrinsic j values for the neutral gas (purple triangles) and stellar (blue circles) components. The j value shown here is calculated directly from the individual gas and star particles respectively. In the case of the neutral gas component, j was calculated from all gas particles weighted by their neutral gas fraction. The Fall relation, as derived by Posti et al. (2018), is shown by the purple line and accompanying shaded region. Below 10^8 $M_*(\mathrm{M}_\odot)$, the gas component has higher j relative to the stellar component, while above this mass, the gas and stellar components share a common disc and have similar j.

The difference between the gas and stellar components could be due to dynamical heating of stellar populations after formation, or by the formation of stars occurring within lower-angular-momentum gas which has collapsed further towards the centre of the galaxy. Alternatively, this may also be due to the low baryonic particle numbers in the simulation, leading to a disproportionate transfer of heat from the dark matter halo to the baryonic component. While the consistency between our results for TNG50, TNG100 and TNG300 suggest that this may not be a dominating factor, higher resolution simulations will be helpful in removing this uncertainty.

5.2. The cause of the jump in j_*

In this subsection we consider possible causes of the jump in j: resolution effects, galaxy mergers, bursty star formation and the accretion mode of gas. When following the evolution of j_* back through time in the simulation, we found that while all galaxies initially lose angular momentum over time, some then experience a significant and sometimes very rapid rise to a higher angular momentum state. Once in this state, these galaxies then maintain a relatively constant j_*, while those which do not experience this jump continue to lose angular momentum. Distributions of the star and gas components show that this jump corresponds to the formation of a stable rotating disc.

It may be possible that this is due to the resolution of the simulation, with stable discs appearing once the galaxy passes a certain mass threshold, and hence a certain particle number threshold in the simulation. However, we found that the jump in j_* occurs over a wide range of particle numbers, suggesting that it isn't triggered by a certain particle number limit. The fact that the final j_* values of our simulation sample, resulting from this divergent evolution, closely agree with our observational measurements also supports a physical nature for these different evolutions of j_*.

https://doi.org/10.1017/pasa.2026.10248 Published online by Cambridge University Press

Galaxy mergers can have a significant and rapid effect on a galaxy's angular momentum. In particular, gas-rich ('wet') mergers can significantly increase j_* (Lagos et al. 2018). Cadiou et al. (2022) also found that certain merging configurations can lead to a very sudden rise in j_* followed by a stable period. However, while some of our galaxies do experience minor and major merger events, many of those which experience a rapid rise in j_* do not show any signs of mergers. They are isolated galaxies at the centres of their own group halos, and their tracks through space-time show no dynamical motions caused by the pull of any nearby galaxy. Therefore mergers or interactions with neighbouring galaxies are not the cause of the transition in j_* that we see.

Bursty star formation has been suggested as being disruptive for discs due to the short periods of intense star formation and associated winds and radiation (Gurvich et al. 2023). The formation of a disc may therefore correspond to a transition to a smoother, more continuous rate of star formation. An initial investigation into the star formation activity in our simulation galaxies showed no significant change in the variability of star formation during the time in which they transition to a state of higher angular momentum, though this should be investigated more carefully in future work.

Hopkins et al. (2023) showed using the FIRE simulations that a change in the shape of the gravitational potential corresponds to the formation of a disc. More specifically, when the central matter concentration of the galaxy increases beyond a certain point, the circular velocity profile changes from a profile which initially increases with radius to one which is decreasing with radius. We therefore investigated if there was a correlation between the sudden increase in j_* we see in IllustrisTNG and the shape of the total gravitational potential. While we did see a change in the circular velocity profile at the same time as the jump in some cases, we did not see such a correlation across the full sample of simulated galaxies.

The source and nature of gas falling into the central regions of the galaxy also potentially plays an important role. The initial gas inflow is thought to be in the form of high-angular-momentum cold gas accretion (Stewart et al. 2013), which is often not aligned with the angular momentum of the dark matter halo, leading to a decrease in the overall specific angular momentum of the baryons during this phase (Stewart 2017; Hafen et al. 2022). The stellar population forming out of this gas would subsequently also have a low specific angular momentum. As the galaxy increases in mass, a hot, virialised gaseous halo forms around the galaxy, acquiring the angular momentum of the host halo. Gas then falls into the centre isotopically from this hot halo and cools, creating a more constant, uniform source of gas inflow with aligned angular momentum onto the inner galaxy (Hafen et al. 2022). This gas carries the angular momentum of the outer halo into the central regions of the galaxy, forming a high-angular-momentum disc.

The recent study by Benavides et al. (2025), carried out using the FIREBox simulation (a cosmological simulation with a volume of 22.1 $cMpc^3$), identified a transition region between low-mass dispersion-dominated systems and high-mass disc-dominated systems within the stellar mass range of $10^9 < M_* < 10^{10}$ $M_\odot$. Within this region the fraction of stars on disc-like orbits increased, which was taken as an indication of disc formation. This transition corresponded to a transition from bursty to steady star formation, a deepening of the gravitational potential and the formation of a hot gaseous halo, all of the main factors discussed above. While Benavides et al. (2025) found the end of bursty star formation to most strongly correlate with the beginning of disc formation, all three factors likely play a role in the formation of a disc and an associated rise in j_*. Similarly, while we didn't find any of these processes to play a singular role in the transformation seen in this work, a combination of all three may work together to create the transition in j_* and allow the formation of a disc.

Interestingly, Benavides et al. (2025) found the transition range to occur an order of magnitude above the range where we have observed an increase in j_* in this work ($10^8 < M_* < 10^9$ $M_\odot$. This could indicate that the transition in j_* begins before disc formation becomes evident in other parameters; however a consistent comparison would need to be made between these simulations for these findings to be compared more directly.

5.3. Implications for the understanding of galaxy angular momentum

Our finding that the low-mass star-forming dwarf galaxies follow the same relation as that of the high-mass disc galaxies suggests that the process of angular momentum build-up through tidal torques, and the subsequent transfer and conservation of this angular momentum to the baryonic component, continues to be independent of the galaxy mass down to stellar masses of 10^6 $M_*(M_\odot)$. This suggests that the high dark matter fraction, shallow potential wells (and subsequently more significant impacts of feedback processes) does not significantly alter the transfer and conservation of angular momentum within the baryonic component. This continuation of the relation, as found for high-mass disc galaxies, is also in spite of the fact that the lowest mass dwarfs in our sample have disordered, irregular morphologies. This may not be expected, as for galaxies above 10^9 $M_*(M_\odot)$, many studies have found significant offsets in the j_*–M_* relation with morphology (as detailed in the Introduction), with elliptical and bulge-dominated galaxies having lost angular momentum relative to (and after their transformation from) disc-dominated galaxies. Despite their chaotic structure and turbulent kinematics, irregular galaxies evidently retain a significant amount of their halo's original angular momentum within their central star-forming components.

In terms of the evolution of j_* with time, previous studies have shown the subsequent evolution can have a significant impact on the angular momentum initially imparted on halos through tidal torques; in particular, merger events which disrupt the disc/s and transform it into an elliptical galaxy greatly reduce the coherent rotational motion of the stars and result in a significant decrease in j_*. It is evident from Section 4.6 that high-mass disc galaxies also have a very varied and dynamic evolution in j_*, yet despite this complexity, star-forming galaxies which maintain their disc morphology fall into a tight j_*–M_* relation by the present day.

6. Summary and conclusion

In this work we aimed to determine if the relationship between a galaxy's mass and specific angular momentum (j_*), known as the Fall relation, extends down to the low-mass dwarf galaxies. To achieve this, we studied 49 star-forming dwarf galaxies and 20 high-mass control galaxies observed by the SHαDE survey and measured their specific angular momentum from Hα-derived velocity maps and continuum-derived mass distributions. We found that our high-mass control galaxies follow the same relation as found for Posti et al. (2018),

https://doi.org/10.1017/pasa.2026.10248 Published online by Cambridge University Press

showing the consistency of our tracer with previous studies. We further found that our dwarf galaxy sample continues to follow this relation down to $10^{5.7}\,M_*(\mathrm{M}_\odot)$, with an increase in scatter below $10^8\,M_*(\mathrm{M}_\odot)$. For our complete sample, we find $\alpha = 0.53 \pm 0.04$ and $\beta = 3.23 \pm 0.11$. The continuity in the relation to low masses, at least in the case of star-forming dwarf galaxies, supports the idea that the buildup of angular momentum in galaxies is scale-free, with the high dark matter fraction and shallow gravitational potential wells not having a significant effect on the build-up and conservation of angular momentum in the baryonic component through the galaxy formation process. We find a correlation in the residual of the relation with star formation rate, with higher j values being associated with higher star formation rates; by analogy with the high-mass galaxy population, quenched dwarf galaxies will likely be offset from the observed relation.

We then followed up these findings with an investigation into dwarf galaxies in the IllustrisTNG-50 cosmological simulation. To make a direct comparison with our observational results, we used the star-forming gas particles in each galaxy to create flux and kinematic maps resembling the SHαDE observations. We then applied the same methods to the simulated observations to determine an observationally-equivalent value of j_*. We found that while the simulated low-mass dwarfs also generally follow the extended Fall relation, with a flattening of the relation and increased scatter towards lower-j_* values below $10^9\,M_*(\mathrm{M}_\odot)$. This may be caused by the resolution limitations of the simulations, with lower-mass galaxies being resolved by too few particles. However, we note that we find consistency in this distribution when we perform the same analysis using the lower resolution TNG100 and TNG300 simulations. Within the simulation, we then confirm that the angular momentum of the star-forming gas follows that of the stellar component in general, and that the neutral gas as a whole has a higher value of j relative to the stars. This latter result, along with previous observational studies including Catinella et al. (2023) and the fact that Hα is less extended relative to HI, explains why we find lower j values using Hα compared to previous HI studies of dwarf galaxy angular momentum. We then followed the simulated galaxies back through their evolutionary history. We found that while all galaxies initially lose angular momentum with time, some galaxies experience a sudden and often rapid increase in j_* when they are within the stellar mass range of 10^8–$10^9\,M_*(\mathrm{M}_\odot)$ before settling into a steady state with a relatively constant value of j_*. This transition may also be due to resolution limitations of the simulation, though we note that the same transition, in the same mass range, is found in the lower-resolution TNG100 simulation.

Assuming a physical origin, we investigated many potential mechanisms for this sudden change in j_* experienced by the higher-mass galaxies, but were unable to conclusively determine a single cause of this change. The transition is likely caused by a combination of factors including a change in the burstiness of star formation, deepening gravitational wells and a change in the mode of gas accretion. In order to fully investigate this transition, high-resolution optical observations of dwarf galaxies are needed in the stellar mass range of 10^8–$10^9\,M_*(\mathrm{M}_\odot)$, along with resolved HI observations allowing for the velocity mapping of the surrounding HI gas. Such observations would provide great insight into what causes a galaxy to undergo a state change in specific angular momentum, and potentially reveal the conditions necessary for the formation of discs in galaxies. No matter what the cause may be, the apparent simplicity and tightness of the Fall relation in the present day, observed here over 5 orders of magnitude in stellar mass, belies a complex and dynamic evolution of j_*.

Acknowledgements. SD and SMS acknowledges funding from the Australian Research Council (DE220100003). LC acknowledges support from the Australian Research Council Discovery Project funding scheme (DP210100337). Parts of this research were conducted by the Australian Research Council Centre of Excellence for All Sky Astrophysics in 3 Dimensions (ASTRO 3D), through project number CE170100013. We would like to thank Aaron Romanowsky and Pavel E. Mancera Piña for helpful discussions on this paper. We thank the reviewer for helpful feedback which improved the paper.

References

Aihara, H., et al. 2018, PASJ, 70, S4
Barat, D., et. al. 2020, MNRAS, 498, 5885
Benavides, J. A., et al. 2025, arXiv:2508.00991
Boselli, A., et al. 2014, A&A, 564, A67
Bournaud, F., Jog, C. J., & Combes, F. 2007, A&A, 476, 1179
Bruzual, G., & Charlot, S. 2003, MNRAS, 344, 1000
Butler, K. M., Obreschkow, D., & Oh, S.-H. 2017, ApJL, 834, L4
Cadiou, C., Pontzen, A., & Peiris, H. V. 2022, MNRAS, 517, 3459
Camps, P., & Baes, M. 2015, A&C, 9, 20
Cappellari, M. 2023, MNRAS, 526, 3273
Catinella, B., et al. 2023, MNRAS, 519, 1098
Celiz, B. M., et al. 2025, A&A, 699, A12
Chabrier, G. 2003, PASP, 115, 763
Chowdhury, A., & Chengalur, J. N. 2017, MNRAS, 467, 3856
Cortese, L., et al. 2016, MNRAS, 463, 170
Croom, S. M., et al. 2021, MNRAS, 505, 991
Dale, D. A., et. al. 2023, AJ, 165, 260
Davies, R. L., et. al. 1983, ApJ, 266, 41
De Lucia, G., et. al. 2006, MNRAS, 366, 499
Deeley, S., et. al. 2021, MNRAS, 508, 895
Dey, A., et al. 2019, AJ, 157, 168
Diemer, B., et al. 2018, ApJS, 238, 33
Doroshkevich, A. G. 1970, Afz, 6, 581
Du, M., Ho, L. C., Yu, H.-R., & Debattista, V. P. 2022, ApJL, 937, L18
Efstathiou, G., & Jones, B. J. T. 1979, MNRAS, 186, 133
Elson, E. C. 2017, MNRAS, 472, 4551
Elson, E., Glowacki, M., & Davé, R. 2023, NewA, 99, 101964
Fall, S. M. 1983, IAUS, 100, 391
Fall, S. M., & Romanowsky, A. J. 2018, ApJ, 868, 133
Foreman-Mackey, D., et al. 2013, ascl.soft. ascl:1303.002
Genel, S., et al. 2015, ApJL, 804, L40
Green, A. W., et al. 2018, MNRAS, 475, 716
Groves, B., et al. 2008, ApJS, 176, 438
Gurvich, A. B., et al. 2023, MNRAS, 519, 2598
Hafen, Z., et al. 2022, MNRAS, 514, 5056
Hardwick, J. A., et al. 2022, MNRAS, 516, 4043
Hardwick, J. A., et al. 2023, MNRAS, 526, 808
Hopkins, P. F., et al. 2023, MNRAS, 525, 2241
Hoyle, F. 1949, Problems of Cosmical Aerodynamics, ed. J. M. Burgers, & H. C. van de Hulst (Dayton: Central Air Documents Office), 195
Kennicutt, R. C. 1998a, ApJ, 498, 541
Kennicutt, R. C. 1998b, ARA&A, 36, 189
Kurapati, S., et al. 2018, MNRAS, 479, 228
Lagos, C. d. P., et al. 2017, MNRAS, 464, 3850
Lagos, C. d. P., et al. 2018, MNRAS, 473, 4956
Mancera Piña, P. E., et al. 2021a, A&A, 647, A76
Mancera Piña, P. E., et al. 2021b, A&A, 651, L15
Marinacci, F. et al. 2018, MNRAS, 480, 5113
McGaugh, S. S., Schombert, J. M., & Lelli, F. 2017, ApJ, 851, 22

https://doi.org/10.1017/pasa.2026.10248 Published online by Cambridge University Press

Mostoghiu, R., et al. 2021, A&A, 652, A10
Murugeshan, C., et al. 2021, MNRAS, 507, 2949
Naiman, J. P̃., et al. 2018, MNRAS, 477, 1206
Nelson, D. et al. 2018, MNRAS, 475, 624
Nelson, D., et al. 2019a, MNRAS, 490, 3234
Nelson, D., et al. 2019b, ComAC, 6, 2
Obreschkow, D., & Glazebrook, K. 2014, ApJ, 784, 26
Peebles, P. J. E. 1969, ApJ, 155, 393
Pillepich, A. et al. 2018, MNRAS, 475, 648
Pillepich, A., et al. 2019, MNRAS, 490, 3196
Posti, L., et al. 2018, A&A, 612, L6
Renzini, A., & Peng, Y.-J. 2015, ApJL, 801, L29
Rodriguez-Gomez, V., et al. 2019, MNRAS, 483, 4140
Rodriguez-Gomez, V., et al. 2022, MNRAS, 512, 5978
Romanowsky, A. J., & Fall, S. M. 2012, ApJS, 203, 17
Springel, V. et al. 2018, MNRAS, 475, 676
Stewart, K. R., et al. 2013, ApJ, 769, 74
Stewart, K. R. 2017, ASSL, 430, 249
Sweet, S. M., et al. 2018, ApJ, 860, 37
Sweet, S. M., et al. 2020, MNRAS, 494, 5421
White, S. D. M. 1984, ApJ, 286, 38
Zavala, J., et al. 2016, MNRAS, 460, 4466
Zhou, L., et al. 2017, MNRAS, 470, 4573

Appendix A

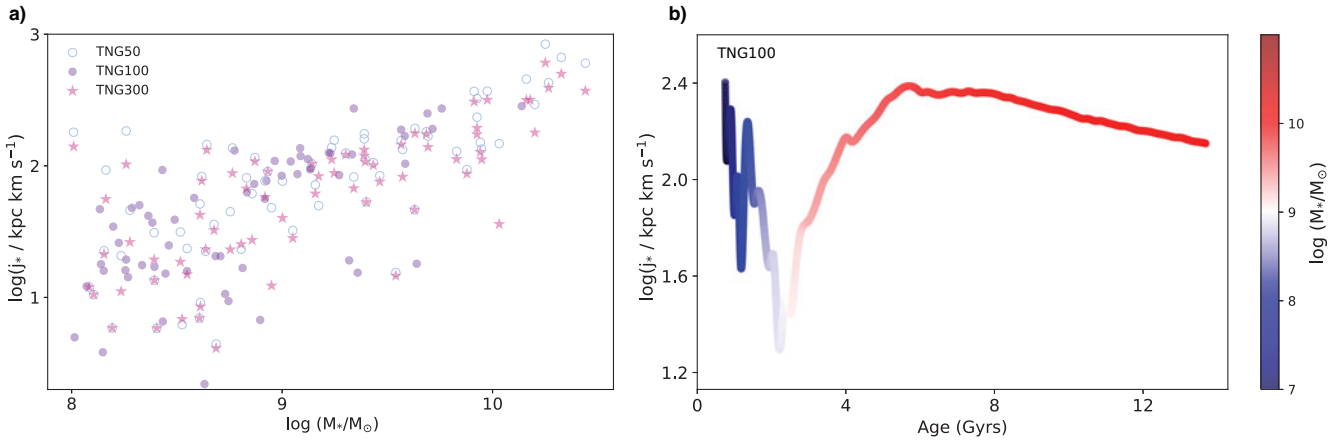


Figure A1. Consistency with TNG100 and TNG300 as a test of potential resolution effects. (a) shows the *j*-M plot for a random sample of galaxies in TNG50 (blue), TNG100 (purple) and TNG300 (magenta). The distribution of galaxies within the *j*-M plane is consistent, including the increasing scatter towards lower *j* values below 10^9 $M_*(M_\odot)$. (b) shows an example of a galaxy within TNG100 experiencing a rapid increase in *j* just below 10^9 $M_*(M_\odot)$, also consistent with TNG50 despite the lower resolution of TNG100. This suggests that the rapid jump within the 10^8–10^9 $M_\odot$ mass range is more likely to be a physical effect rather than a resolution effect.

https://doi.org/10.1017/pasa.2026.10248 Published online by Cambridge University Press